

# <sup>1</sup> High-Resolution Spatiotemporal Monitoring of Secondary Microseisms via Multi-Array Analysis

<sup>3</sup> Yajian Gao<sup>1</sup>, Andreas Rietbrock<sup>1</sup>, Frederik Tilmann<sup>2,3</sup>, Edmond Dushi<sup>4</sup>

<sup>1</sup> *Geophysical Institute, Karlsruhe Institute of Technology, Karlsruhe, Germany*

<sup>2</sup> *GFZ Helmholtz Centre for Geosciences, Potsdam, Germany*

<sup>3</sup> *Freie Universität Berlin, Berlin, Germany*

<sup>4</sup> *Institute of Geosciences, Polytechnic University of Tirana, Tirana, Albania*

<sup>4</sup> 19 December 2025

## <sup>5</sup> SUMMARY

<sup>6</sup> This study presents a workflow to monitor spatiotemporal variations of the secondary micro-  
<sup>7</sup> seisms using multi-array analysis. We employ ambient-noise cross-correlation beamforming  
<sup>8</sup> (CC beamforming) across three dense seismic networks with different instrument responses:  
<sup>9</sup> ANTICS in Albania (nodal-geophone and broadband), Hi-net in Japan (short-period), and  
<sup>10</sup> SCSN (broadband) in Southern California. Independent of their instrumentation, these net-  
<sup>11</sup> works enable us to track the spatial and temporal evolution of secondary microseism sources  
<sup>12</sup> in the northern Hemisphere from autumn 2022 to spring 2023. The workflow involves contin-  
<sup>13</sup> uous data preprocessing for different instrumented sensors, ambient-noise cross-correlation,  
<sup>14</sup> beamforming, and beam-power back-projection into a global map. We also propose sliding-  
<sup>15</sup> window raw-data beamforming (RA beamforming) for the continuous broadband data in this  
<sup>16</sup> workflow to record the absolute amplitudes of secondary microseisms recorded by ANTICS.  
<sup>17</sup> Joint CC beamforming analysis across the three different networks improves the resolution of  
<sup>18</sup> ambient-noise source localization and displays high consistency with the equivalent vertical  
<sup>19</sup> force at the ocean floor. The results indicate that secondary microseism sources in the northern

20 Hemisphere are predominantly driven by winter storms in the northern Atlantic and north-  
21 ern Pacific. The relative and absolute amplitudes of the beam-power for the northern Atlantic  
22 are also extracted from CC beamforming based on geophone sensors and RA beamforming  
23 based on broadband instruments from ANTICS, respectively. Both approaches provide robust  
24 estimates of microseism strength in the northern Atlantic, with CC beamforming displaying a  
25 higher correlation with the modeled ocean floor equivalent forces.

26 This study confirms the feasibility of using cost-effective nodal seismic arrays for detailed  
27 monitoring of secondary microseisms and highlights the potential for integrating multi-array  
28 seismic data with oceanographic models for an improved understanding of seismic noise gen-  
29 eration and propagation.

30 **Key words:** Secondary microseism Ambient Noise Beamforming

## 31 1 INTRODUCTION

32 Seismic ambient noise has been studied thoroughly over the last few decades, and significant  
33 success has been achieved involving the extraction of empirical Green's functions for seismic  
34 tomography, most often surface wave tomography involving mapping the thickness and properties  
35 of sedimentary layers, the crust, and even the upper mantle (e.g. Shapiro et al. 2005; Shen et al.  
36 2013). Less common are studies which extract seismic body waves from ambient noise cross-  
37 correlation, for example, to map the mantle discontinuities (e.g. Poli et al. 2012; Pedersen et al.  
38 2022; Lu et al. 2023) and global propagation and imaging (e.g. Boué et al. 2013; Boué et al. 2014;  
39 Boué & Tomasetto 2023).

40 Even earlier, the heterogeneous distribution and physical nature of ambient noise sources were  
41 studied (e.g. Longuet-Higgins 1950; Chevrot et al. 2007; Kedar et al. 2008; Arduin et al. 2011;  
42 Liu et al. 2016). Natural seismic noise is dominated by sources generated in the oceans (e.g.  
43 Arduin et al. 2015; Tanimoto & Anderson 2023). Its amplitude is highest in the microseism band  
44 (3–30 s), which is generally subdivided into primary and secondary microseisms according to their  
45 dominant periods.

46 The primary microseism dominates in the period band from 10 to 30 s, whereas the secondary

47 microseism contributes mainly to the noise between 3 and 10 s (Peterson 1993; Arduin et al. 2015;  
48 Tanimoto & Anderson 2023). Primary microseisms are generated where pressure fluctuations from  
49 ocean waves interact with variations in seafloor bathymetry, typically in shallow-water regions  
50 (e.g., Bromirski et al. 2017; McNamara & Boaz 2019). They occur at the same frequency as the  
51 generating ocean waves (single-frequency microseisms) and thus carry information about near-  
52 shore and coastal wave dynamics. In contrast, secondary microseisms have twice the frequency of  
53 incoming ocean waves (Longuet-Higgins 1950) due to the non-linear interaction of two opposing  
54 ocean wave trains with similar dominant periods (e.g. Longuet-Higgins 1950; Hasselmann 1963;  
55 Nakata et al. 2019). The secondary microseisms also usually display the most energetic amplitude  
56 in the seismic ambient noise spectrum (e.g. Peterson 1993; Nakata et al. 2019; Liu et al. 2024).  
57 Though the depth range of ocean waves is confined to the upper 100-200 m, the pressure associated  
58 with the standing wave caused by wave-wave interaction can exert pressure at any depth below  
59 where two interacting wave trains meet at the sea surface. Therefore, this process can generate  
60 seismic waves at the ocean floor (Gualtieri et al. 2014, 2015; Tomasetto et al. 2025; Tanimoto &  
61 Anderson 2023).

62 Secondary microseisms can be caused by three types of physical wave configurations (Obreb-  
63 ski et al. 2012; McNamara & Boaz 2019). The strongest type of secondary microseism source  
64 comes from the interaction of two ocean wave systems that have the same dominant frequency but  
65 opposite directions (e.g. Arduin et al. 2011; McNamara & Boaz 2019; Li et al. 2020). This type  
66 often occurs in the open ocean when one ocean swell meets the opposite ocean waves from another  
67 swell, which could be previously generated by the same storm or uncorrelated storms (e.g. Obreb-  
68 ski et al. 2012). The two other sources are related to oblique ocean waves that meet the main wave  
69 direction as well as the interaction of the incoming ocean waves with the reflected waves from  
70 the coastline (Arduin et al. 2011; Arduin & Roland 2012). All three mechanisms can create a  
71 pressure wave that propagates down to the ocean floor. The direct P (pressure wave) in the water  
72 layer, the reflected P at the ocean floor, and the refracted P (along the ocean floor and then return-  
73 ing into the water layer), all could be further amplified by multiple reflections at the sea surface  
74 (Gualtieri et al. 2015; Nakata et al. 2019). Even though a large part of the energy remains within

75 the water layer, a part of the energy can be transmitted across the sea floor into the solid earth as  
76 body waves, i.e., the transmitted P and P-to-S converted wave. The sum of multiple reflected P  
77 waves in the water layer can generate frequency-dependent resonance effects in the source region,  
78 which are called 'source site effect' (Gaultieri et al. 2013, 2014, 2015). In addition to body waves,  
79 Rayleigh and Love waves can be generated beneath the ocean floor through coupling, conversion,  
80 and resonance effects. In this study, we focus on the body wave, especially the P wave. For a more  
81 detailed derivation of the excitation of the surface wave from secondary microseism, readers are  
82 referred to Longuet-Higgins (1950); Arduin et al. (2011); Stutzmann et al. (2012); Tomasetto  
83 et al. (2025) for Rayleigh waves, and Gaultieri et al. (2020); Xiao et al. (2021) for Love waves.  
84 The efficiency of this conversion from ocean acoustic waves to elastic waves beneath the ocean  
85 floor is thus influenced by the water depth, the slope of the sea floor, and the sediment thickness  
86 (Nakata et al. 2019; Gaultieri et al. 2013, 2014, 2015; Liu et al. 2020).

87 Thanks to significant efforts in developing the oceanographic hindcast model WAVEWATCHIII  
88 (WW3) by IFREMER (Tolman et al. 2014), it is possible to roughly compare the significant wave  
89 height and spectral density of the wave-induced pressure just below the sea surface (hereafter, sur-  
90 face spectral density) with the location of ambient noise sources from seismological observations  
91 (e.g., Igel et al. 2021; Xiao et al. 2021; Li et al. 2020; Farra et al. 2016; Nishida & Takagi 2016).  
92 However, significant wave height or ocean spectral density (WW3 hindcast model) should not be  
93 used directly as a proxy for the ambient noise source because coupling and resonance are not taken  
94 into account. The recent systematic ambient noise reconstruction package Wave Model Sources  
95 of Ambient Noise (WMSAN) (Tomasetto et al. 2025) reformulates and summarizes the synthetic  
96 ambient noise physics based on WW3 products. WMSAN additionally considers bathymetry and  
97 wave-induced pressure in the water column. WMSAN could help seismologists reconstruct syn-  
98 thetic secondary microseism source maps, synthetic spectrograms and synthetic cross-correlations  
99 with considerations of different seismic wave types (e.g., P, SV and Rayleigh waves). Therefore,  
100 in this study, we explore the application of these recent developments to the calculation of the  
101 synthetic secondary microseism generation (equivalent force) on the ocean floor and compare it  
102 with the secondary microseism observations from multiple datasets.

103 However, secondary microseism source information is typically embedded within continuous  
104 seismic recordings together with regional and teleseismic earthquakes and anthropogenic noise  
105 (Lecocq et al. 2020). Extracting the location and strength of secondary microseism sources is  
106 therefore a central challenge for spatiotemporal microseism analysis. Several approaches have  
107 been proposed to address this problem. These include temporal amplitude analysis of seismic  
108 records (Ardhuin et al. 2011), beamforming-based methods (e.g., Gal et al. 2015; Koper et al.  
109 2009; Nishida & Takagi 2022; Euler et al. 2014), elliptical polarization analysis (e.g., Koper &  
110 Hawley 2010; Lu et al. 2021), and adjoint full-waveform inversion (FWI) applied to ambient-  
111 noise cross-correlations, primarily for Rayleigh waves (Sager et al. 2018; Igel et al. 2021). In most  
112 cases, the inferred microseism source characteristics are subsequently compared with oceano-  
113 graphic proxies such as significant wave height or surface pressure spectral density derived from  
114 the WAVEWATCH III (WWIII) model. Among these approaches, raw-data beamforming (RA  
115 beamforming) and back-projection are widely used for detecting ambient-noise sources but typi-  
116 cally require explicit exclusion of earthquake-contaminated time windows and spectral whitening  
117 to suppress transient seismic signals and local cultural noise (e.g. Gal et al. 2015; Xiao et al.  
118 2021; Nishida & Takagi 2022). In contrast, cross-correlation beamforming (CC beamforming)  
119 offers an alternative strategy that inherently suppresses incoherent transient signals through cross-  
120 correlation and enables flexible time-windowing and station-pair selection (Euler et al. 2014).  
121 The diagonal elements of the cross-spectral density matrix correspond to auto-correlation spectra  
122 and can be excluded, preventing bias from incoherent noise that would otherwise contaminate the  
123 beamforming results. For a detailed comparison between conventional RA beamforming and CC  
124 beamforming, the reader is referred to Euler et al. (2014) and Ruigrok et al. (2017).

125 In this study, we try to extract robust ambient noise cross-correlations for three different instru-  
126 mented networks, including broadband, short-period (Nishida & Takagi 2016), and geophone-type  
127 (Cheng et al. 2021) seismometer recordings, and apply CC beamforming to track the evolution of  
128 secondary microseisms. For all recording types, we are able to generate 3-hourly and daily sec-  
129 ondary microseism maps. We further perform multi-array CC beamforming, which combines the  
130 individual maps. The results are further compared with the secondary microseism from SANS

## 6 *Yajian Gao*

model (Igel et al. 2021), significant wave heights, surface spectral densities from WW3, and the ocean-floor equivalent forces calculated using WMSAN (Tomasetto et al. 2025), which directly predicts the strength of microseisms generated, accounting for source site effects. Our multi-array CC beamforming can better constrain the spatiotemporal evolution of the secondary microseism (5-10 s) in the northern hemisphere with 3-hourly resolution and correlates well with the computed secondary microseism generation on the ocean floor (WMSAN). To further analyze the temporal changes in the strength of the secondary microseism in the northern Atlantic, we extract the relative and absolute beam-power amplitudes from the ANTICS data as a function of time over 9 months. CC beamforming performs better than RA beamforming in constraining the winter secondary microseism in the northern Atlantic when the Mediterranean Sea is also experiencing enhanced storm activity affecting the regional noise field.

## 142 **2 DATA**

143 In this study (Figure 1), we analyze continuous seismic waveform data from the permanent  
144 short-period Hi-net array (Okada et al. 2004; Obara et al. 2005) in Kyushu, Japan, the broadband  
145 stations from Southern California Seismic Network (SCSN, California Institute of Technology  
146 (Caltech) (1926)), and the recent dense nodal-array in Albania (ANTICS - "AlbaNian TectonIcs  
147 of Continental Subduction", (Agurto-Detzel et al. 2025a)) which was operated jointly by the Karl-  
148 sruhe Institute of Technology, Helmholtz Centre for Geosciences (GFZ) and Polytechnic Univer-  
149 sity Tirana, Albania (PUT). ANTICS consisted of 332 4.5-Hz natural-frequency and 3-component  
150 geophones and 50 broadband stations covering an area of 150 km by 150 km. These three networks  
151 provide sufficient data coverage and balanced sensitivity to reconstruct the microseism source map  
152 in the northern Atlantic and northern Pacific.

## 153 **3 METHOD**

154 We use a simple workflow for extracting the spatiotemporal variations of the secondary mi-  
155 croseisms from the ambient noise CC beamforming for three seismic networks (Euler et al. 2014).  
156 We also retrieve temporal relative and absolute amplitude changes of secondary microseisms in

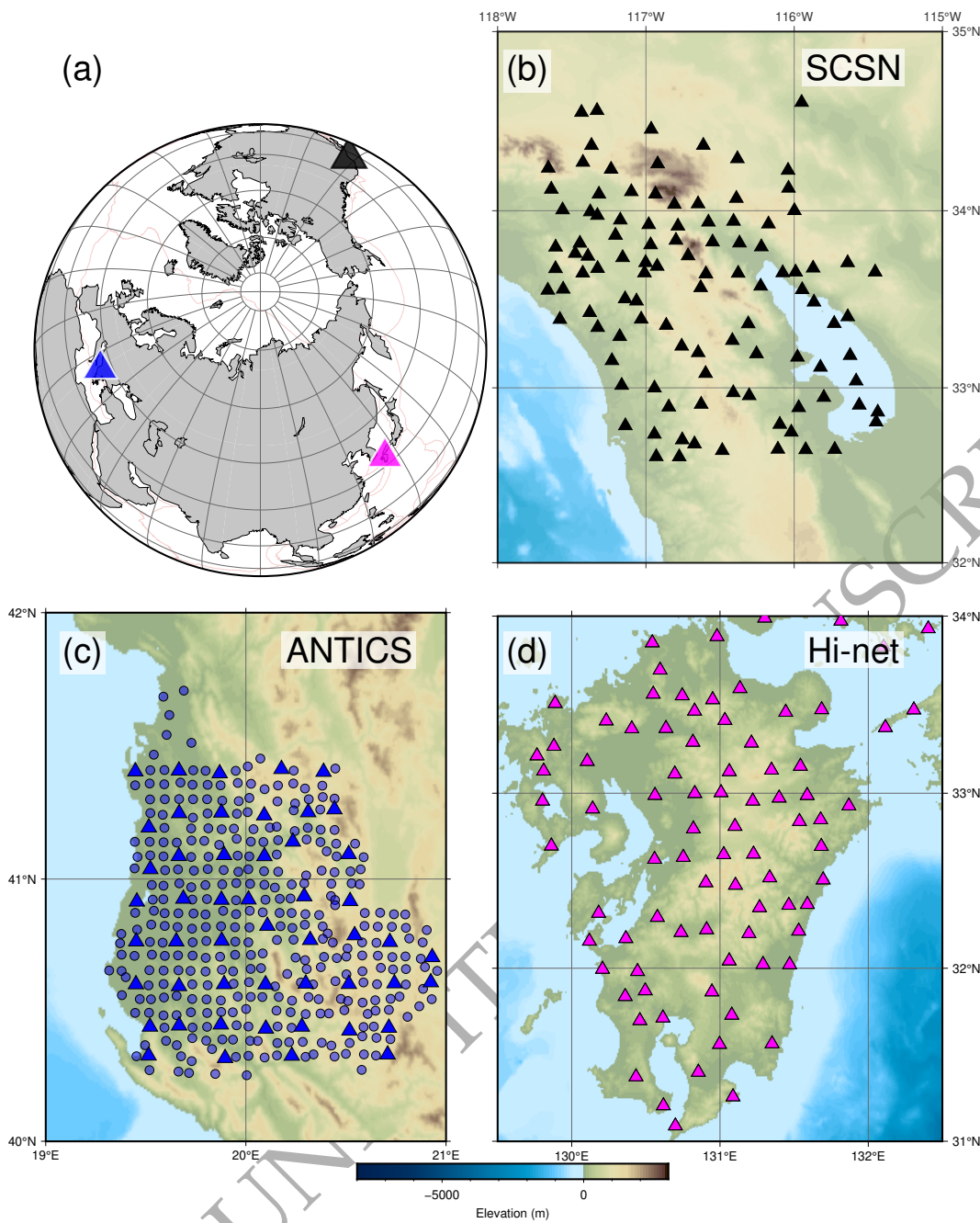


**Figure 1.** Map for three dense seismic networks: (a): Global view for three networks;(b) Southern California Seismic Network (SCSN, network code CI) (c) ANTICS (Blue triangles denote Broadband seismometers, whereas blue circles represent nodal-array geophones, network code X3) (d) Hi-net short-period instruments (network code N).

157 the northern Atlantic. CC beamforming is applied to the time series from 322 geophone stations  
 158 of ANTICS, whereas the conventional sliding-window (150 s) RA beamforming is applied on the  
 159 continuous velocity recordings from the 50 broadband stations (Le Pape et al. 2021). The whole  
 160 workflow for both methods is summarized in Fig. 2.

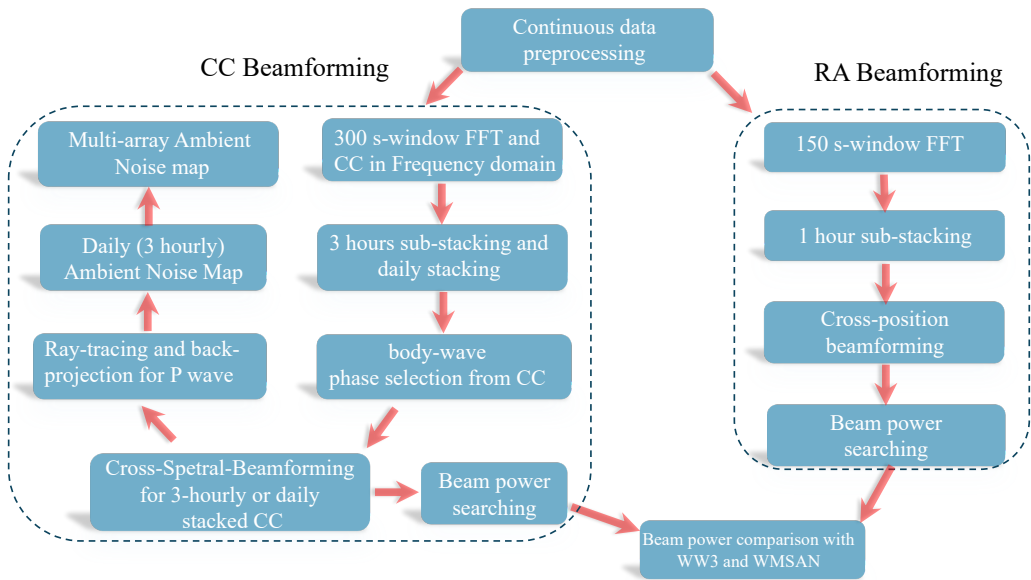


**Figure 2.** Workflow for retrieval of secondary microseisms from ambient noise CC beamforming and RA beamforming. CC beamforming is applied on three networks to jointly map the location of secondary microseisms and relative amplitude extraction for the geophones from ANTICS, whereas the RA beamforming is applied for the ANTICS broadband stations to extract the absolute amplitude of secondary microseisms in the northern Atlantic.

### 161 3.1 Data Preprocessing and Ambient Noise Cross-Correlation

162 For broadband stations (SCSN and the ANTICS broadband subset), the instrument response  
 163 is removed to obtain ground velocity, ensuring reliable amplitude scaling within the 0.1–0.2 Hz  
 164 (5–10 s) microseism band used for absolute beam-power analysis (RA beamforming for the AN-  
 165 TICS broadband subset). In contrast, the Hi-net short-period sensors and ANTICS nodal-array  
 166 geophones have natural frequencies of 1 and 4.5 Hz, respectively. Deconvolving these responses  
 167 to displacement or velocity at 0.1–0.2 Hz would amplify instrument noise and produce unstable  
 168 long-period artifacts. Therefore, these data were kept in raw counts. Importantly, the short-period  
 169 and nodal arrays are used only in CC beamforming, where amplitudes are normalized and the rel-  
 170 ative source localization, not absolute scaling, is the objective. Consequently, absolute amplitude  
 171 comparisons are restricted to the broadband networks. For the CC beamforming, we then cut the  
 172 continuous seismic data into 300 s time segments (non-overlapping) and down-sample the data to  
 173 10 Hz. We use time-frequency domain whitening to remove the transient signals caused by earth-  
 174 quakes or other disturbances. Cross-correlations are calculated individually for all three networks

(Fig. 3a,c,e). In this work, we use NoisePy (Jiang & Denolle 2020) to adopt two-step spectral whitening that includes the running mean average (RMA) in the frequency domain (10 points in the frequency domain) and set the absolute amplitude of the complex Fourier spectrum to 1. The spectrally whitened continuous waveforms are then cross-correlated (see equation 1) for station pairs in the Fourier domain. In the frequency domain, the cross-correlation can be written as:

$$R(x^i, x^j, \omega) = v(x^i, \omega) \cdot v^*(x^j, \omega) \quad (1)$$

where  $v(x^i, \omega)$  are the pre-processed vertical time series in the frequency domain recorded at location  $x_i$  and  $*$  denotes the complex conjugate. The correlation function  $R(x^i, x^j, \omega)$  is calculated for  $i \neq j$ , i.e., all auto-correlations are excluded. Therefore,  $n(n - 1)/2$  unique station pairs are included.

3-hourly stacks of cross-correlation traces ( $\pm 150$  s time lags are saved) for 36 segments are calculated to suppress transient signals and saved locally for further daily stacking and beamforming (Fig. 3a,c,e).

### 3.2 CC Beamforming and RA beamforming

Different from conventional beamforming, CC beamforming (Rugrok et al. 2017) requires that the data are first cross-correlated for all possible receiver pairs (see section above). The beam power, therefore, can be expressed as:

$$B(p, \theta, \omega) = \left| \sum_{k=1}^{n(n-1)/2} R(\omega, x_k^i, x_k^j) \exp [I\omega d^k p \cos(\theta^k - \theta)] \right| \quad (2)$$

Here  $d^k$  and  $\theta^k$  denote the receiver-pair distance and azimuth, respectively. The  $k$  denotes the receiver-pair index.  $p$  and  $\theta$  represents the slowness and backazimuth (baz), respectively, for frequency-wavenumber scanning.  $I$  denotes the imaginary unit.

The equation above provides a way to calculate beam power for cross-correlation waveforms. Before the beam power is calculated, the teleseismic P wave window in the cross-correlation waveforms has to be selected with an apparent velocity larger than 6.5 km/s to mute the Rayleigh waves

(Fig. 3a,c,e). The beam power for multiple frequency values is then averaged over the period range 5–10 s. Rayleigh waves dominate ambient noise in this frequency band but primarily represent local surface oscillations rather than the teleseismic body-wave microseisms targeted here (Fig. 3b,d,f). Muting them enhances the coherence of the P-wave arrivals and prevents contamination from strong near-surface energy.

In contrast, the beam power from RA beamforming (Gal et al. 2015; Koper et al. 2009; Nishida & Takagi 2022) is calculated directly from the velocity traces.

$$B(p, \theta, \omega) = \sum_{t=1}^N \left| \sum_{k=1}^n v_t(x^k, \omega) \exp [I\omega d^k p \cos(\theta^k - \theta)] \right| \quad (3)$$

Here,  $d^k$  and  $\theta^k$  denote the relative distance and azimuth with respect to the center of the array, respectively. The  $k$  denotes the receiver index. The outer summation denotes the summation over  $N$  sliding time windows, with  $t$  the window index. Since the seismograms are analyzed directly, we use a window length of 150 s to minimize contamination from transient earthquake signals and local disturbances, while still ensuring adequate frequency resolution in the 5–10 s band. Therefore, 24 segments are stacked hourly. The beam power for multiple frequency values is then averaged, as for CC beamforming over the period range 5–10 s.

### 3.3 Array response function

The array response function (ARF) describes how an array of sensors responds to a plane wavefield emanating from a particular direction or originating from a specific point source. The ARF encapsulates the phase and amplitude variations across the array elements, fundamentally influencing the beamforming output. Understanding the ARF is crucial for optimizing array configurations and beamforming algorithms to achieve the desired resolution and directivity characteristics. This subsection focuses on the comparative analysis of two prominent beamforming methods: RA beamforming and CC beamforming for three networks, respectively.

For the RA beamforming, the ARFs of the three networks display many small artifacts in the beam pattern image (Fig. A1), whereas the CC beamforming generates cleaner beam patterns and suffers less from non-coherent signals (Fig. A2). For HINET, the beam pattern from RA

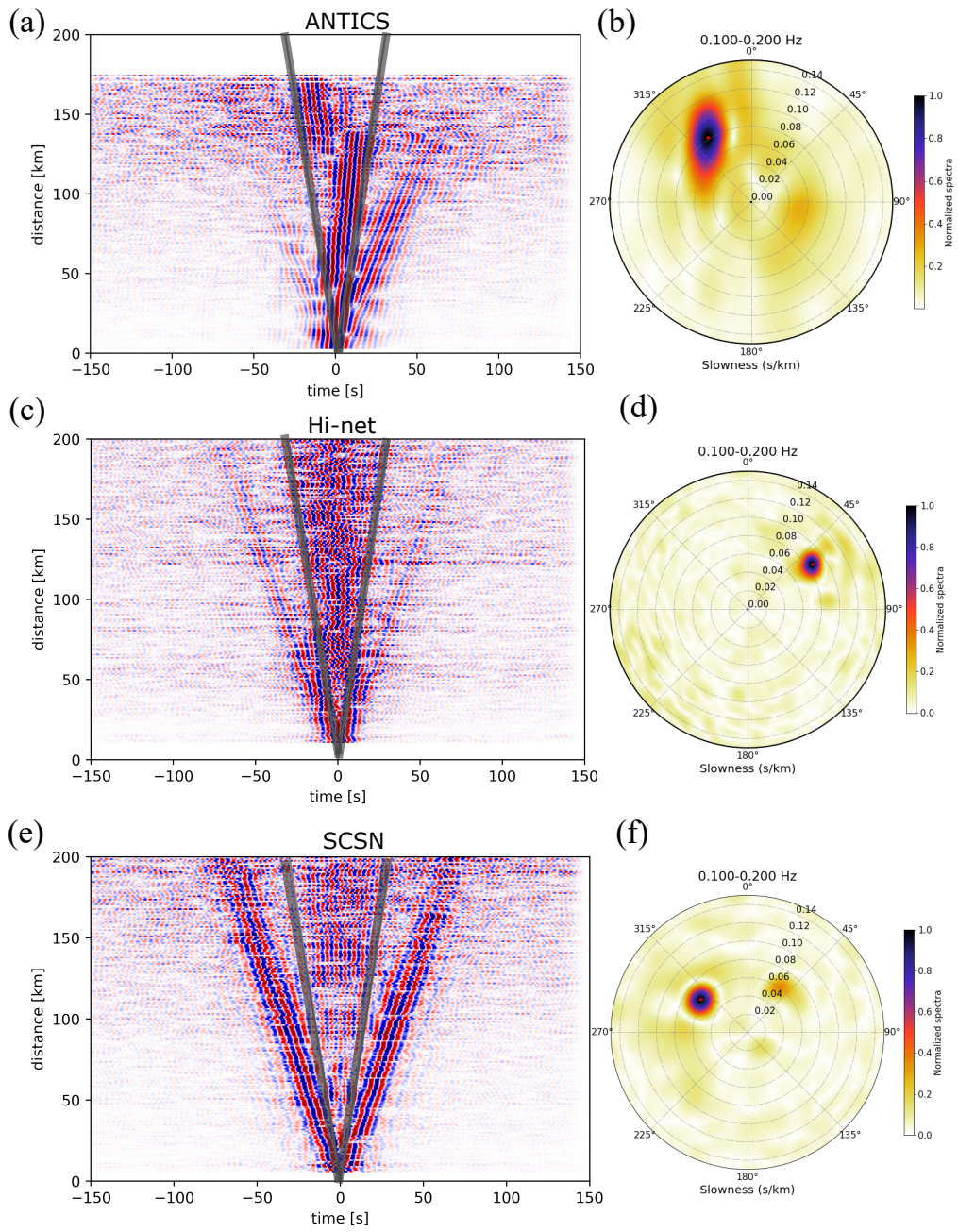


**Figure 3.** a,c,e: Ambient noise cross-correlation daily stacking for 2022-11-18 from three networks (filtered from 5 to 10 s); The thick gray dashed lines illustrate the reference velocity of 6.5 km/s. b,d,f: Beamforming of the cross-correlations shown on the left for the band 5-10 s. The outer limit of the circles corresponds to an apparent velocity of 6.5 km/s, as visualised by the gray line on the left.

beamforming shows spurious secondary maxima for the 5 and 8-s beam patterns (Fig. A1). For ANTICS, due to the small aperture, the resolution deteriorates for lower frequencies and suffers from smearing in the slowness direction in the CC beamforming pattern (Fig. A2).

Quantitative resolution estimates from the array response functions (Fig. A1–A2) demonstrate the differing capabilities of the three networks. The -3 dB (half-power) azimuthal beamwidths are approximately 20°–36° for ANTICS (depending on period), 12°–22° for SCSN, and 10°–18° for Hi-net at slowness 0.15 s/km. These values highlight how the smaller aperture of ANTICS leads to broader main lobes and reduced azimuthal resolution, whereas the large-aperture permanent arrays produce narrower beams. Nevertheless, the dense station spacing of ANTICS provides superior spatial coherence and sensitivity to short-wavelength, low-amplitude microseisms, particularly valuable in the Adriatic–Mediterranean region where local sources may dominate. The CC beamforming pattern (Fig. A2) also shows significantly reduced sidelobe energy relative to RA beamforming, confirming that CC beamforming enhances coherent body-wave retrieval and overall source-localization accuracy. These quantitative results underscore the complementary roles of dense nodal and sparse arrays in the multi-array analysis presented here.

### 3.4 Teleseismic P wave ray-tracing and back-projection

We use teleseismic P-phase energy to construct the beamforming and back-projection spectra. The direct P wave is the dominant phase within an epicentral distance of 25°–90°, corresponding to slowness values of 5–10 s/° (Euler et al. 2014). This range captures coherent body-wave energy from the northern Atlantic and Pacific storms that reach our three northern Hemisphere arrays during winter.

The PP phase occupies a similar but partially overlapping slowness band (4.4–9.5 s/°), yet its amplitude is generally smaller than that of the direct P wave for distances <100° (including Pdiff). For larger distances (100°–125°), the PP phase may become stronger but shares comparable slowness (7–8 s/°) with the P wave at 50–65° epicentral distance (Gerstoft et al. 2008). To avoid ambiguity between these overlapping phases, we assume that only the direct P wave contributes significantly to the beam power within 25°–90°.

249 Other teleseismic phases such as Pdiff, PcP, PKPab–bc, PKiKP, and PKIKP can also con-  
 250 tribute energy to the beamforming spectrum. Among these, Pdiff ( $90^\circ$ – $110^\circ$ ) is back-projected as  
 251 an extension of P. The PKPab and PKPbc branches form an arc in the slowness–distance domain  
 252 ( $2$ – $4.5$  s/° for  $130^\circ$ – $152^\circ$ ), causing phase ambiguity; therefore, only PKPbc is considered. PKiKP  
 253 and PKIKP are included to represent the farthest observable distances ( $>152^\circ$ ).

254 **3.5 Modeling ocean floor equivalent force**

255 Based on the spectral density of the wave-induced pressure from the WW3 model (Tolman  
 256 et al. 2014), we further inferred ambient noise source strength (equivalent vertical force F at the  
 257 sea floor, Fig 4h) in the secondary microseism band from 5 to 10 s. The equivalent vertical force  
 258 F applied at the ocean floor is calculated by considering the amplification coefficients for the P  
 259 wave (source site effects) following Retailleau & Gualtieri (2021) and Tomasetto et al. (2025).  
 260 The amplification coefficient is related to the thickness of the ocean layer (bathymetry); therefore,  
 261 we utilize a global bathymetry model at 30 arc-min resolution to match the same spatial resolution  
 262 of the WW3 model (Tolman et al. 2014; Tomasetto et al. 2025).

263 The amplification coefficient can be expressed as below:

$$c_P(f, h) = \sqrt{\int_0^{\theta_{Pw}^*} \left| \frac{T_P(\theta_{Pw})}{1 + R(\theta_{Pw}) \exp(i\phi_w(h(r), 2\pi f, \theta_{Pw}))} \right|^2 d\theta_{Pw}} \quad (4)$$

264 where  $f$  is the seismic frequency in Hz (twice the ocean wave frequency);  $h$  is the ocean depth  
 265 in m;  $\theta_{Pw}$  denotes the P-wave takeoff angle range;  $\phi_w$  is the plane P-wave potential propagating  
 266 in water;  $R$  is the seabed interface reflection coefficient and  $T_P$  is the seabed interface P-wave  
 267 transmission coefficient.

268 The equivalent vertical force F could be expressed as:

$$F = 2\pi \sqrt{\int_{-\pi/2}^{\pi/2} \int_0^{2\pi} \int_{f_{min}}^{f_{max}} c_P^2(\lambda, \phi, f_s) F_p R_E^2 \cos \lambda d\lambda d\phi df} \quad (5)$$

269 where  $F_p$  is the spectral density just below the sea surface in  $\text{Pa}^2 \text{m}^2 \text{s}$  from the WW3 model.  
 270  $f_{min}$  and  $f_{max}$  denote lower and upper frequency bounds in Hz. In this study, we only focus on the  
 271 period band from 5 to 10 s (secondary microseism period band), therefore,  $f_{min} = 0.1$  Hz and  $f_{max}$

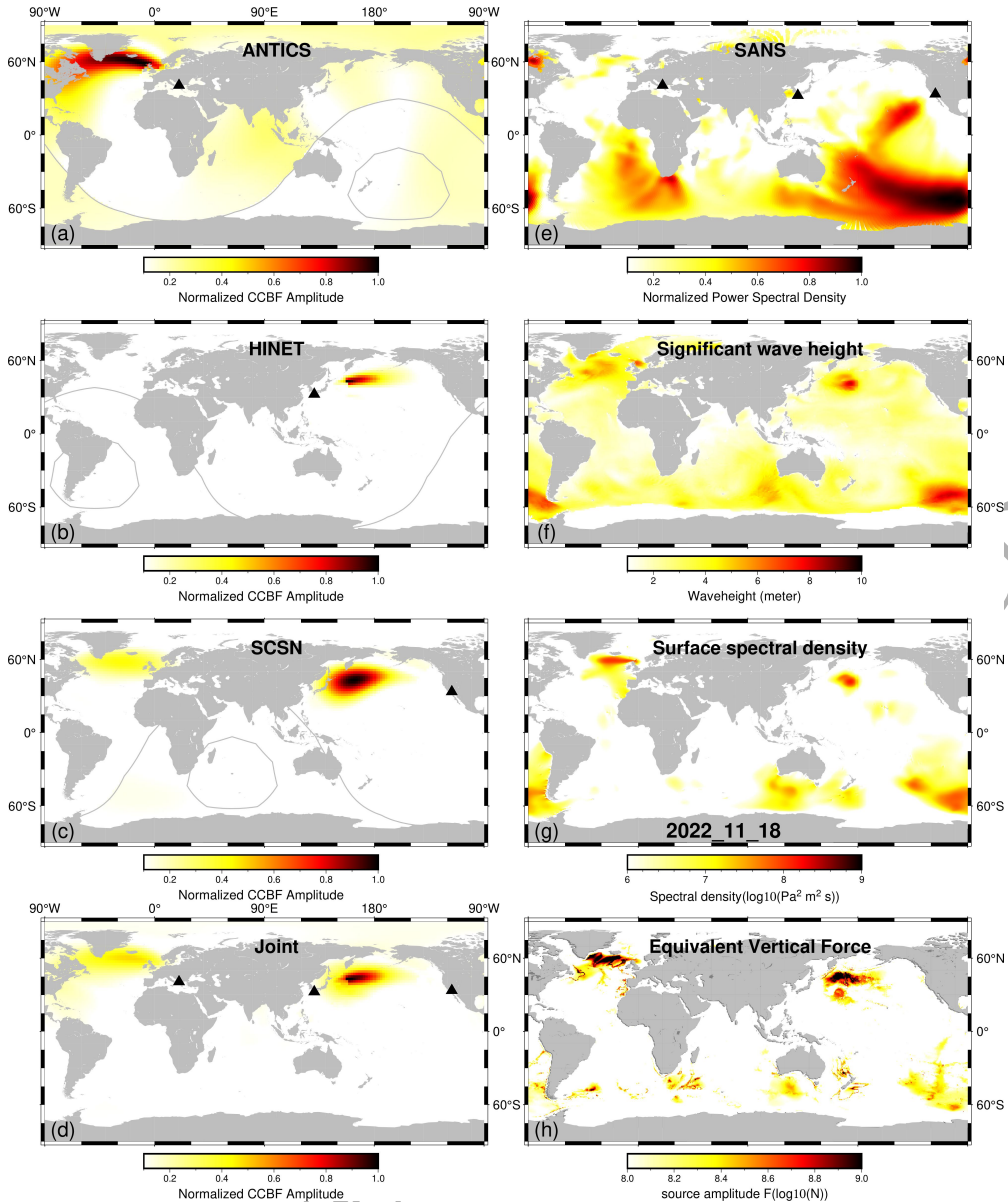


**Figure 4.** (a-c) Cross-correlation beam power and back-projection for three individual networks; gray curves in (a)-(c) denote epicentral distances of  $90^\circ$  and  $120^\circ$ . (d) Joint back-projection constraints from the three networks. (e) Seismic Ambient Noise Source (SANS) maps from full waveform inversion (Igel et al. 2021). (f) daily averaged wave height map on 2022-11-18 and (g) daily averaged surface spectral density at 5-10 s, as extracted from WW3 model. (h) Equivalent vertical force on the ocean floor considering the source site effects and assuming body wave propagation, reconstructed using WMSAN from Tomasetto et al. (2025).

<sup>272</sup>  $= 0.2$  Hz.  $R_E$  is the Earth's radius in m.  $\lambda$  and  $\phi$  represent the latitude and longitude in degrees.

<sup>273</sup> For details on the computation, see Gualtieri et al. (2014); Tomasetto et al. (2025).

274 **3.6 Beam power estimation**

275 To explore the relationship among the beam power of a single seismic array, significant wave  
 276 height, and the equivalent force of the ocean floor, we utilize the ANTICS array to extract the  
 277 temporal variation of beam power from the CC beamforming in the northern Atlantic. We search  
 278 for the maximum beam power within the northwestern baz ( $270^\circ$  - $360^\circ$ ) and teleseismic P wave  
 279 slowness ( $6$  -  $10$  s $^\circ$ ). We then compare the strength with the maximums of significant wave height  
 280 from WW3 (Ardhuin et al. 2010), and the equivalent force for the P wave on the ocean floor (Fig.  
 281 5).

282 To extract the absolute beam power amplitude, we also applied the RA beamforming (Fig.  
 283 2) to the 50 broadband seismometers of the ANTICS. As the nodal stations only have a corner  
 284 frequency of 4.5 Hz and to minimize computational cost, we only try to extract the absolute beam  
 285 power from the ANTICS broadband stations and search for the maximum beam power in the  
 286 northern Atlantic direction (the same search criterion as CC beamforming).

287 **4 RESULTS AND DISCUSSION**288 **4.1 Spatial and temporal variations of the secondary microseism locations**

289 In this study, we focus on the continuous evolution of secondary microseisms extracted from  
 290 joint ambient noise CC beamforming from the autumn of 2022 to the spring of 2023. We explore  
 291 the robustness of monitoring secondary microseisms using three dense seismic arrays with dif-  
 292 ferent instrumentation for the northern Hemisphere. The high-density ANTICS nodal array (3 km  
 293 inter-station spacing) provides superior spatial coherence and enables robust beamforming even for  
 294 short-wavelength (0.1–0.2 Hz) microseisms. Although its smaller aperture yields a broader -3 dB  
 295 beamwidth ( $18^\circ$  at 8s, see ARF in Fig A2 and A1) than Hi-net and SCSN ( $12^\circ$ ) and decreases the  
 296 spatial resolution for multiple sources and low-frequency signals, the dense geometry enhances the  
 297 signal-to-noise ratio and sensitivity to the microseism in the northern Atlantic and Mediterranean  
 298 Sea. Conversely, the sparse wide-aperture permanent networks achieve finer azimuthal resolution  
 299 but lower coherence for weak signals. The complementary combination of dense regional nodal

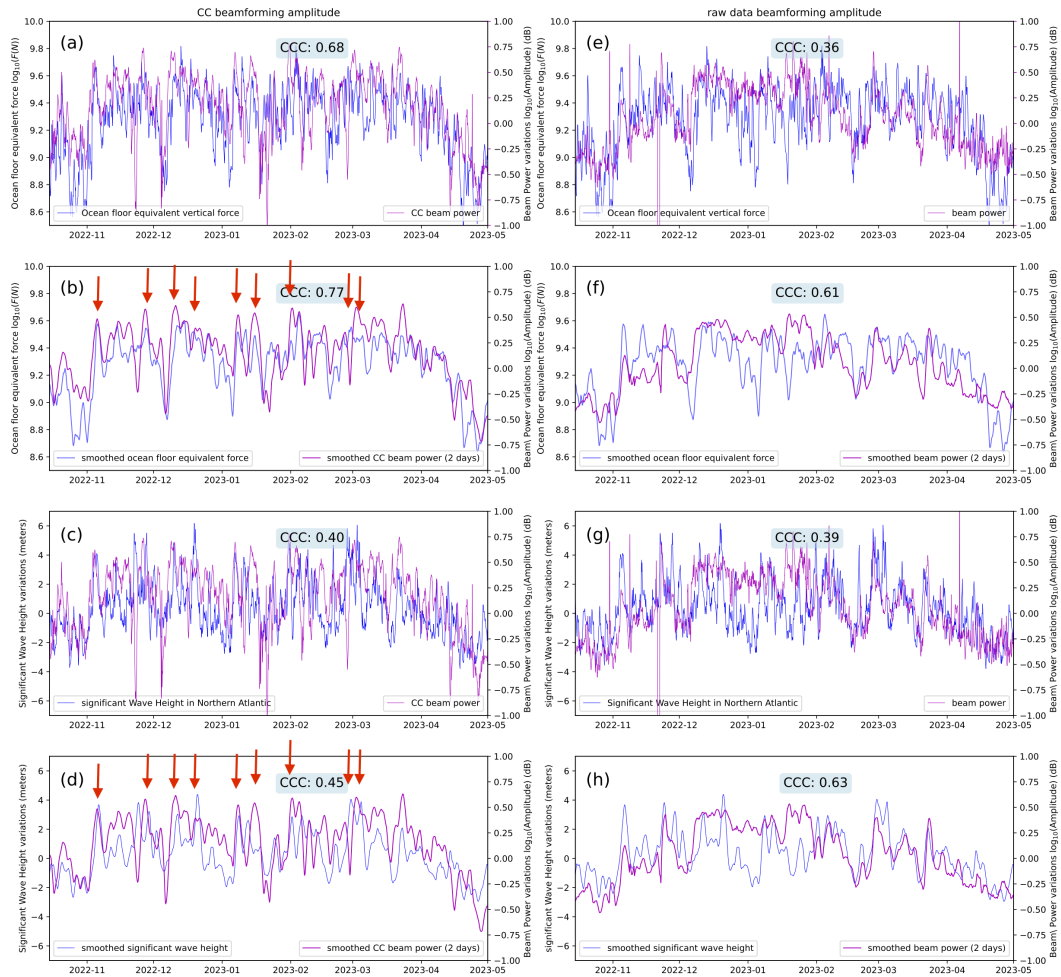


**Figure 5.** Comparison of beam power from CC beamforming (Left) and RA beamforming (Right) with ocean floor equivalent force and significant wave height for the northern Atlantic. (a) 3-hourly maximum equivalent force and relative beam power retrieved from CC beamforming. (b) 2-days averaged maximum equivalent force and relative beam power (16 points median smoothing). (c) 3-hourly significant wave height and relative beam power. (d) 2-days averaged maximum significant wave height and cc beam power (16 points median smoothing). (e) to (h) are equivalent comparisons of oceanographic variables with absolute beam power from RA beamforming. The red arrows in b and d denote significant storms in the northern Atlantic.

300 arrays and large-aperture networks thus enables multi-scale tracking of microseism sources across  
301 oceanic basins.

302 In the daily cross-correlations on 2022-11-18 for the ANTICS network (Fig. 3), the body wave  
303 signals with apparent velocities greater than 6.5 km/s are stronger than the surface waves and  
304 show significant amplitude differences between the left and right branches. For this case, the right  
305 branch shows stronger amplitudes at shorter interstation distance (0-130 km) than the left branch  
306 but at larger interstation distance (120-170 km), the left branch is much stronger (Fig 3a). After  
307 applying CC-beamforming, ANTICS displays strong beam power around  $315^{\circ}$  in baz and  $0.08$   
308  $\text{s}/\text{km}$  ( $8.9 \text{ s}^{\circ}$ ) in slowness, indicating that the dominant plane wave comes from the northwest,  
309 likely from the Atlantic.

310 On the same day, the cross-correlation body wave phases are rather weaker and more diffused  
311 on Hi-net and SCSN. For Hi-net, the left branch shows relatively stronger amplitudes than the right  
312 branch. The beamforming for Hi-net indicates that the dominant signal comes from the northeast.  
313 Meanwhile, SCSN displays a rather symmetric cross-correlation, and beamforming denotes that  
314 the dominant signal comes from the northwest and a weaker signal from the northeast. Considering  
315 the geographic location of Hi-net and SCSN, we can infer that the most influential signal for both  
316 networks comes from the same source. The dominant signal from the northwest in the ANTICS  
317 originates from another source, which likely corresponds to the weak signal with northeastern baz  
318 on the SCSN beam power plot.

319 Through the back-projection (Fig. 4), we can easily identify the locations of the microseisms.  
320 The contributing teleseismic energy captured by ANTICS mainly comes from the northern At-  
321 lantic (Fig. 4a). The wave height map and surface spectral density from the WW3 model (Ardhuin  
322 et al. 2010) shows two groups of storms between North America and Europe on this day (Fig  
323 4f-g), one located in the northern Atlantic covering a large area and another spatially concentrated  
324 one in the North Sea. At the same time, the SCSN back-projection also captured the same ambient  
325 noise source (Fig. 4c) within the northern Atlantic covering a similar area as determined by AN-  
326 TICS. For the northern Pacific, ANTICS only reveals very weak beam power, presumably because  
327 of the large distance from the source to ANTICS. SCSN and Hi-net detect the same strong and

328 focused ambient noise source south of the Kamchatka Peninsula and east of Japan. Due to the  
329 larger distance to SCSN, the beam power is spread over a wider area than in the Hi-net stack (Fig.  
330 4b). We normalized, linearly summed, and then averaged the beam powers for the three networks  
331 to stabilize the result and improve the resolution. The joint observations (Fig. 4d) provide higher  
332 consistency with the significant ocean wave height (Fig. 4f) and surface spectral density (Fig. 4g)  
333 compared to the single-array beamformings. Fig. 4e shows the global daily ambient noise map  
334 from Rayleigh wave FWI (SANS Igel et al. 2021) for comparison, which exhibits higher lateral  
335 smearing.

336 However, the significant wave height and WW3 ocean surface spectral density only reflect  
337 the ocean weather near the open ocean surface without consideration of the transmission to the  
338 crust and the effect of bathymetry as an amplification coefficient; in other words, neither directly  
339 represents the distribution of the physics of secondary microseism generation. To account for this  
340 physical mechanism and the ocean–solid Earth coupling, we apply a further modulation of the  
341 WW3 spectra using the WMSAN (Tomasetto et al. 2025). This converts the surface spectral den-  
342 sity into a proxy for the equivalent vertical force (P wave) at the seafloor by integrating the non-  
343 linear pressure spectral density and including bathymetry-dependent amplification coefficients for  
344 body waves. The resulting model (Fig 4h) represents the effective ocean floor forcing responsible  
345 for P wave secondary microseisms and better reproduces the observed beam-power amplitude and  
346 timing. The modeled sources are mainly located in the northern Atlantic and northern Pacific with  
347 reduced contributions from the southern hemisphere (Fig.4h) compared to the wave height map  
348 (Fig.4f) and the surface spectral density (Fig.4g), therefore, the modeled sources are more consis-  
349 tent with our observation than surface spectral density and wave height. During our study period  
350 (autumn 2022–spring 2023), northern Hemisphere storm systems dominate secondary microseism  
351 generation. In contrast, Southern Hemisphere sources are not detected, which we attribute to both  
352 seasonal variability and array distribution. The austral summer months produce relatively weaker  
353 microseisms around Antarctica compared to the intense boreal winter storms in the northern At-  
354 lantic and northern Pacific (Gerstoft et al. 2008; Li et al. 2020). In addition, all three arrays used  
355 here are located in the northern Hemisphere, making them far less sensitive to Antarctic sources,

356 which would need to propagate over distances exceeding 120–150°. At such path lengths, attenuation  
357 and interference between different seismic phases in the 5–10 s band further reduce de-  
358 tectability (Retailleau & Gaultieri 2021). This explains why Southern Hemisphere contributions  
359 are negligible in our observations.

360 To further retrieve the temporal variations, we directly compute our 3-hourly substacks of the  
361 cross-correlations for the whole period and repeat the beamforming and back-projection process  
362 for the whole dataset. On the same day of 2022-11-18, the microseism in the northern Atlantic ex-  
363 panded westward progressively from the west coast of Great Britain and Ireland to the east coast  
364 of Canada (Fig. A3a-c). The surface spectral density from the WW3 model also displays a similar  
365 pattern (Fig. A3g-i). However, we should note that a new oceanic storm was generating near the  
366 east coast of Canada, which is more obvious in the significant wave height map (Fig A3e-f), lead-  
367 ing to a gradually broader microseism zone in the northern Atlantic with roughly three hours de-  
368 lay relative to the significant wave height (Fig. A3a-f). On 2022-11-19 the new oceanic storm near  
369 Canada became stronger, migrated eastwards very quickly (Fig A4d-f) and dominated the northern  
370 Atlantic on 2022-11-20 (Fig A5d-f), leading to the significantly high microseism amplitudes on  
371 2022-11-20 (Fig A5a-c,j-l). In contrast, the microseism in the northern Pacific was generated by a  
372 unique storm system and was moving eastward very slowly, then separated into two small storm  
373 systems (Fig A4d-f) and gradually died out on 2022-11-20 (Fig A5a-c). This temporal correspon-  
374 dence suggests that the nonlinear coupling between opposing wave systems strengthens during the  
375 mature stage of storm evolution, constraining the development timescale of wind-wave systems  
376 to roughly the period over which microseism amplitudes rise to their maximum. A complete spa-  
377 tiotemporal evolution of the secondary microseism generation from 2022-10-01 to 2023-05-01 is  
378 visualised in the supplementary video.

379 In summary, these exemplary comparisons demonstrate that our CC beamforming using mul-  
380 tiple arrays can capture and constrain the spatiotemporal evolution of secondary microseisms with  
381 unprecedented resolution, at least in the northern hemisphere. The multi-array approach can sig-  
382 nificantly reduce the smearing effects of a single array and avoids the interferences caused by  
383 other seismic phases. The direct comparison with WMSAN equivalent-force modeling links the

<sup>384</sup> predicted nonlinear ocean-solid earth coupling from wave models to higher-resolution real obser-  
<sup>385</sup> vations.

<sup>386</sup> **4.2 Temporal strength variations of secondary microseism in the northern Atlantic**

<sup>387</sup> Because different data types and beamforming methods can yield different representations of  
<sup>388</sup> microseism sources, we next evaluate how well each approach and each subdataset of ANTICS  
<sup>389</sup> (nodal-geophone and broadband seismometer) captures the strength of the secondary microseism  
<sup>390</sup> Retailleau et al. (2018) and compare the results with modeled equivalent-force variations in the  
<sup>391</sup> northern Atlantic derived from WMSAN. This comparison tests the physical consistency between  
<sup>392</sup> observed seismic power at a specific baz direction range and the nonlinear ocean-wave interactions  
<sup>393</sup> that generate secondary microseisms. It clarifies the advantages and limitations of the CC and RA  
<sup>394</sup> beamforming methods.

<sup>395</sup> Based on the two types of datasets from ANTICS and two different beamforming methods, the  
<sup>396</sup> relative and absolute amplitudes of secondary microseisms in the northern Atlantic are retrieved  
<sup>397</sup> through a grid-search to find the local maximum (northern Atlantic direction) in the beam power  
<sup>398</sup> patterns. In order to obtain stable estimate, the rolling median within a 6-hour time window is taken  
<sup>399</sup> to represent the microseism strength in that time window. First, outliers, which are mostly related  
<sup>400</sup> to large amplitudes, from teleseismic or local earthquakes, are removed. Outliers are identified  
<sup>401</sup> using the 10th and 90th percentiles of the distribution: the inter-percentile range ( $IPR = Q90 - Q10$ )  
<sup>402</sup> is taken as a robust measure of variability. Any value lying outside ( $Q10-IPR, Q90+IPR$ ), i.e., a  
<sup>403</sup> range corresponding to three times the  $IPR(10-90)$ , is considered an outlier and removed (Fig. A6).  
<sup>404</sup> The resulting gaps are closed by forward-filling before calculating the 6 h rolling mean. Finally,  
<sup>405</sup> a longer rolling mean (48 samples) is applied to the cleaned series to highlight two-day trends  
<sup>406</sup> (Fig 5). For example, the destructive Turkey-Syria earthquake (Mw 7.8) caused significant ground  
<sup>407</sup> motion in Albania, but the IPR preprocessing and further smoothing can alleviate the influence  
<sup>408</sup> on the beam power from the outliers caused by strong earthquakes (Fig. A6). This approach is  
<sup>409</sup> comparable to the traditional IQR method (based on quartiles), but using  $Q10-Q90$  provides a  
<sup>410</sup> wider, more permissive band that reduces false positives in skewed data, where several apparent

411 spikes represent valid signals due to strong storm activity. The procedure preserves the underlying  
 412 microseism variability while reliably discarding short-lived extreme excursions caused by seismic  
 413 activity.

414 Fig. 5 (a) and (e) compare the 3-hourly ocean floor equivalent force with the beam power  
 415 calculated from CC beamforming and RA beamforming. (c) and (g) are the 3-hourly comparisons  
 416 between the beam power and maximum wave height. The two beam power datasets, ocean floor  
 417 equivalent force, and significant wave height time series are smoothed through a rolling mean with  
 418 a window size of 48 hours to retrieve the long-period trends (Fig. 5b,f,d,h).

419 The beam power from CC beamforming shows a higher correlation with the modeled equiva-  
 420 lence force ( $CCC = 0.77$ ) than does RA beamforming for the northern Atlantic ( $CCC = 0.61$ ). Sev-  
 421 eral quiet intervals in the northern Atlantic during the boreal winter (late December–early January  
 422 and late January–early February) are reproduced more faithfully by the CC beamforming results  
 423 (Fig. 5b and f), indicating that CC better suppresses incoherent local or regional noise. In contrast,  
 424 the lower correlation between broadband RA beam power and the modeled equivalent force (and  
 425 wave height) during winter likely reflects elevated noise from local Mediterranean sources. Figs.  
 426 A7–A8 support this interpretation: coastal ANTICS stations exhibit PSD levels up to 15 dB higher  
 427 than inland stations in the 0.1–0.2 Hz band (up to 30 dB for 0.2–1 Hz) and the enhanced mod-  
 428 elled equivalent force near the central Mediterranean Sea and Ionian Sea, demonstrating that local  
 429 bathymetry, shallow-water resonance, and wind-sea activity increase incoherent energy in this fre-  
 430 quency and slowness range. These local contributions primarily affect RA beamforming, whereas  
 431 CC beamforming—by focusing on coherent body-wave arrivals—more accurately tracks open-  
 432 ocean (Atlantic) forcing. Similar conclusions were drawn by Borzì et al. (2025), which showed  
 433 that Mediterranean microseism amplitudes correlate most strongly with local wave heights within  
 434 500 km of the coast and peak during winter when wind-driven sea waves dominate.

435 In summary, the strong temporal agreement between the CC beam power and the modeled  
 436 equivalent force confirms that CC beamforming effectively isolates coherent body-wave micro-  
 437 seism energy generated by nonlinear ocean–wave interactions in the northern Atlantic, separating  
 438 it from near-field noise. The weaker RA correlation reflects additional incoherent local energy,

439 particularly from the Mediterranean. This comparison validates the physical basis of the WM-  
440 SAN framework and underscores the potential of multi-array CC analysis for identifying global  
441 storm-driven body-wave sources. On the other hand, the complementary performance of CC and  
442 RA beamforming indicates that both approaches are valuable for continuous monitoring: CC iso-  
443 lates coherent far-field body-wave energy that best traces large-scale storm activity, whereas RA  
444 beamforming, together with PPSD analysis, preserves absolute amplitude information useful for  
445 assessing local variability and near-field sources with different dominant frequency (Fig.A7). The  
446 dense ANTICS nodal array demonstrates that compact, low-cost deployments can capture these  
447 processes with high spatial coherence, though their broad beamwidth limits azimuthal resolu-  
448 tion compared with large-aperture networks. Consequently, the current multi-array configuration  
449 markedly improves spatial resolution for Northern-Hemisphere storm monitoring compared with  
450 single-array analyses, and future global extensions will benefit from arrays of differing apertures  
451 to reduce directional bias and enhance period-dependent coverage of secondary microseisms.

452 Beyond demonstrating methodological robustness, these results highlight that coherent body-  
453 wave microseisms can serve as quantitative indicators of storm evolution and ocean–seafloor cou-  
454 pling strength. The strong match between modeled forcing and observed CC beamforming ampli-  
455 tudes suggests that dense seismic networks can operate as cost-effective, physics-based sensors for  
456 large-scale ocean monitoring and for improving coupled atmosphere–ocean–solid-Earth models.  
457 The temporal evolution described above shows that secondary microseisms reach their maximum  
458 strength during the mature stage of North Atlantic storms, when opposing wave systems become  
459 established. This pattern implies that nonlinear coupling between wind-generated waves devel-  
460 ops progressively as storms intensify. For detailed investigations of shorter-period microseisms,  
461 especially in nearby seas such as the Mediterranean or Ionian, future studies should incorporate  
462 three-component polarization filtering or wavefield-matching methods. In addition, advanced nu-  
463 merical 3-D acoustic–seismic modeling and inversion should be considered to better capture the  
464 influence of local bathymetry and crustal heterogeneity, particularly near deep trenches and be-  
465 neath the arrays.

466 **5 CONCLUSION**

467 In this study, we propose a new workflow based on ambient noise CC beamforming to track  
 468 the sources of secondary microseism in the northern hemisphere. We applied this technique to  
 469 three differently instrumented networks (ANTICS; SCSN, and Hi-net) for the time period from  
 470 fall 2022 to spring 2023. The teleseismic P phases in the cross-correlation traces are selected  
 471 by slowness range and used for the beamforming and back-projection. The distribution of the sec-  
 472 ondary microseism sources retrieved from our joint beamforming-back-projection has an excellent  
 473 correlation with the location of the sea floor equivalent forces predicted by the WW3-WMSAN  
 474 model, considering the source site effect and bathymetry. The winter oceanic storms in the north-  
 475 ern Atlantic and Pacific prevail over the secondary microseism of the whole northern hemisphere.  
 476 The beam power extracted from the beamforming of the ANTICS data shows that we can predict  
 477 not only the location but also the excitation strengths of the microseism source area. We also note  
 478 that such results can be achieved with inexpensive seismic nodal stations that are normally only  
 479 used for local seismicity (Shearer et al. 2023) and structural ambient noise studies (Cheng et al.  
 480 2021). More detailed storm evolution analysis, including their waxing and waning stages and how  
 481 they relate to the generation efficiency of microseisms, will be expanded in our future work.

482 **6 DATA AND RESOURCES**

483 The ANTICS dataset (Agurto-Detzel et al. 2025b) will be openly available at the GEOFON web  
 484 service (<https://geofon.gfz.de/>) from May 2028 (Network code: X3). The raw waveform of  
 485 Hi-net was downloaded from <https://www.Hi-net.bosai.go.jp> and the raw waveform data  
 486 of SCSN were downloaded from EarthScope Consortium Data Services. The cross-correlations  
 487 for three networks are computed using NoisePy and cross-correlation data could be accessed on  
 488 request. The cross-correlation beamforming and back-projection code and data are published at  
 489 RADAR4KIT (Gao & Rietbrock 2025). The significant wave height is retrieved from <https://data.marine.copernicus.eu/> and the power spectral distribution is accessed from the output  
 490 of the ocean wave WW3 model at <ftp://ftp.ifremer.fr/ifremer/ww3/HINDCAST/SISMO/>.  
 491 The ocean floor equivalent force is calculated based on WW3 model using the Wave Model

493 Sources of Ambient Noise (WMSAN) code retrieved from <https://tomasetl.gricad-pages.univ-grenoble-alpes.fr/ww3-source-maps>.

495 **7 ACKNOWLEDGE**

496 We thank Prof. Joachim Ritter, Prof. Frank Krueger, Thomas Forbriger, Han Xiao, Fabrice Ardhuin  
 497 and Jonas Igel for helpful discussions. Editor Sida Ni, reviewer Qiaoxia Liu and Chris Carchedi  
 498 helped to enhance the clarity of presentation and depth of discussion. The authors gratefully ac-  
 499 knowledge the Earth System Modelling Project (ESM) for funding this work by providing com-  
 500 puting time on the ESM partition of the supercomputer JUWELS Jülich Supercomputing Centre  
 501 (2021) at the Jülich Supercomputing Centre (JSC). The authors also acknowledge that open-source  
 502 visualization and computation Python packages NoisePy, Numpy, SciPy, Matplotlib, ObsPy and  
 503 PyGMT are heavily used to produce the figures in this paper.

504 **REFERENCES**

505 Agurto-Detzel, H., Rietbrock, A., Tilmann, F., Dushi, E., Frietsch, M., Heit, B., Kufner, S.-K., Lindner,  
 506 M., Rama, B., Schurr, B., & Yuan, X., 2025a. The ANTICS Large-N Seismic Deployment in Albania,  
 507 *Annals of Geophysics*, **68**, doi: <https://doi.org/10.4401/ag-9210>.

508 Agurto-Detzel, H., Rietbrock, A., Tilmann, F., Dushi, E., Frietsch, M., Heit, B., Kufner, S.-K., Lindner,  
 509 M., Rama, B., Schurr, B., & Yuan, X., 2025b. AlbaNian TectonIcs of Continental Subduction (ANTICS),  
 510 doi: <https://doi.org/10.35097/d7zbw6eudy728tp3>.

511 Ardhuin, F. & Roland, A., 2012. Coastal wave reflection, directional spread, and seis-  
 512 moacoustic noise sources, *Journal of Geophysical Research: Oceans*, **117**(C11), doi:  
 513 <https://doi.org/10.1029/2011JC007832>.

514 Ardhuin, F., Rogers, E., Babanin, A. V., Filippot, J.-F., Magne, R., Roland, A., van der Westhuyzen, A.,  
 515 Queffeulou, P., Lefevre, J.-M., Aouf, L., & Collard, F., 2010. Semiempirical Dissipation Source Func-  
 516 tions for Ocean Waves. Part I: Definition, Calibration, and Validation, *Journal of Physical Oceanography*,  
 517 **40**, 1917 – 1941, doi: <https://doi.org/10.1175/2010JPO4324.1>.

518 Ardhuin, F., Stutzmann, E., Schimmel, M., & Mangeney, A., 2011. Ocean wave sources of seismic noise,  
 519 *Journal of Geophysical Research*, **116**, C006952, doi: <https://doi.org/10.1029/2011JC006952>.

520 Ardhuin, F., Gualtieri, L., & Stutzmann, E., 2015. How ocean waves rock the earth: Two mech-

521 anisms explain microseisms with periods 3 to 300 s, *Geophys. Res. Lett.*, **42**(3), 765–772, doi:  
522 <https://doi.org/10.1002/2014GL062782>.

523 Borzì, A. M., Cannata, A., Panzera, F., D'Amico, S., Re, C. L., & Aster, R. C., 2025. Microseism Am-  
524 plitude and Wave Power in the Mediterranean Sea (1996–2023), *Journal of Geophysical Research: Solid*  
525 *Earth*, **130**, doi: <https://doi.org/10.1029/2024JB030528>.

526 Boué, P., Poli, P., Campillo, M., Pedersen, H., Briand, X., & Roux, P., 2013. Teleseismic correla-  
527 tions of ambient noise for deep global imaging of the Earth, *Geophys. J. Int.*, **194**, 844–848, doi:  
528 [10.1093/gji/ggt160](https://doi.org/10.1093/gji/ggt160).

529 Boué, P. & Tomasetto, L., 2023. Opportune detections of global p-wave propagation from microseisms  
530 interferometry, *Comptes Rendus. Géoscience*, **355**, 1–16, doi: <https://doi.org/10.5802/crgeos.222>.

531 Boué, P., Poli, P., Campillo, M., & Roux, P., 2014. Reverberations, coda waves and ambient noise: Cor-  
532 relations at the global scale and retrieval of the deep phases, *Earth and Planetary Science Letters*, **391**,  
533 137–145, doi: <https://doi.org/10.1016/j.epsl.2014.01.047>.

534 Bromirski, P. D., Chen, Z., Stephen, R. A., Gerstoft, P., Arcas, D., Diez, A., Aster, R. C., Wiens, D. A.,  
535 & Nyblade, A., 2017. Tsunami and infragravity waves impacting antarctic ice shelves, *Journal of Geo-  
536 physical Research: Oceans*, **122**(7), 5786–5801, doi: <https://doi.org/10.1002/2017JC012913>.

537 California Institute of Technology (Caltech), 1926. Southern California seismic network,  
538 *International Federation of Digital Seismograph Networks. Other/Seismic Network.*, doi:  
539 <https://doi.org/10.7914/SN/CI>.

540 Cheng, F., Xia, J., Ajo-Franklin, J. B., Behm, M., Zhou, C., Dai, T., Xi, C., Pang, J., & Zhou, C., 2021.  
541 High-Resolution Ambient Noise Imaging of Geothermal Reservoir Using 3C Dense Seismic Nodal Array  
542 and Ultra-Short Observation, *Journal of Geophysical Research: Solid Earth*, **126**(8), e2021JB021827,  
543 doi: <https://doi.org/10.1029/2021JB021827>.

544 Chevrot, S., Sylvander, M., Benahmed, S., Ponsolles, C., Lefèvre, J. M., & Paradis, D., 2007. Source  
545 locations of secondary microseisms in western europe: Evidence for both coastal and pelagic sources,  
546 *Journal of Geophysical Research: Solid Earth*, **112**(B11), doi: <https://doi.org/10.1029/2007JB005059>.

547 Euler, G. G., Wiens, D. A., & Nyblade, A. A., 2014. Evidence for bathymetric control on the distribu-  
548 tion of body wave microseism sources from temporary seismic arrays in Africa, *Geophysical Journal*  
549 *International*, **197**, 1869–1883, doi: <https://doi.org/10.1093/gji/ggu105>.

550 Farra, V., Stutzmann, E., Gualtieri, L., Schimmel, M., & Arduin, F., 2016. Ray-theoretical mod-  
551 eling of secondary microseism P waves, *Geophysical Journal International*, **206**, 1730–1739, doi:  
552 <https://doi.org/10.1093/GJI/GGW242>.

553 Gal, M., Reading, A. M., Ellingsen, S. P., Gualtieri, L., Koper, K. D., Burlacu, R., Tkalcic, H., & Hemer,  
554 M. A., 2015. The frequency dependence and locations of short-period microseisms generated in the  
555 Southern Ocean and West Pacific, *Journal of Geophysical Research: Solid Earth*, **120**, 5764–5781, doi:

556 <https://doi.org/10.1002/2015JB012210>.

557 Gao, Y. & Rietbrock, A., 2025. High-Resolution Spatiotemporal Monitoring of Secondary Microseisms  
558 via Multi-Array Analysis, doi: <https://doi.org/10.35097/hr1xtyxjwu1fyfs7>.

559 Gerstoft, P., Shearer, P. M., Harmon, N., & Zhang, J., 2008. Global P, PP, and PKP wave microseisms  
560 observed from distant storms, *Geophysical Research Letters*, **35**(23).

561 Gaultieri, L., Stutzmann, E., Capdeville, Y., Ardhuin, F., M. Schimmel, A. M., & Morelli, A., 2013. Mod-  
562 eling secondary microseismic noise by normal mode summation, *Geophys. J. Int.*, **193**, 1732–1745.

563 Gaultieri, L., Stutzmann, E., Farra, V., Capdeville, Y., Schimmel, M., Ardhuin, F., & Morelli, A., 2014.  
564 Modelling the ocean site effect on seismic noise body waves, *Geophysical Journal International*, **197**,  
565 1096–1106, doi: <https://doi.org/10.1093/gji/ggu042>.

566 Gaultieri, L., Stutzmann, E., Capdeville, Y., Farra, V., Mangeney, A., & Morelli, A., 2015. On the shaping  
567 factors of the secondary microseismic wavefield, *Journal of Geophysical Research: Solid Earth*, **120**,  
568 6241–6262, doi: <https://doi.org/10.1002/2015JB012157>.

569 Gaultieri, L., Bachmann, E., Simons, F. J., & Tromp, J., 2020. The origin of secondary micro-  
570 seism Love waves, *Proceedings of the National Academy of Sciences*, **117**(47), 29504–29511, doi:  
571 <https://doi.org/10.1073/pnas.2013806117>.

572 Hasselmann, K., 1963. A statistical analysis of the generation of microseisms, *Rev. Geophys.*, **1**(2), 177–  
573 210, doi: <https://doi.org/10.1029/RG001i002p00177>.

574 Igel, J., Ermert, L., & Fichtner, A., 2021. Rapid finite-frequency microseismic noise source inversion at  
575 regional to global scales, *Geophys. J. Int.*, **227**, 169–183, doi: <https://doi.org/10.1093/gji/ggab210>.

576 Jiang, C. & Denolle, M. A., 2020. Noisepy: A new high-performance python tool for ambient-noise  
577 seismology, *Seismological Research Letters*, **91**, 1853–1866, doi: <https://doi.org/10.1785/0220190364>.

578 Jülich Supercomputing Centre, 2021. JUWELS Cluster and Booster: Exascale Pathfinder with Modular  
579 Supercomputing Architecture at Juelich Supercomputing Centre, *Journal of large-scale research facilities*, **7**(A138), doi: <https://doi.org/10.17815/jlsrf-7-183>.

580 Kedar, S., Longuet-Higgins, M., Webb, F., Graham, N., Clayton, R., & Jones, C., 2008. The origin of  
581 deep ocean microseisms in the North Atlantic Ocean, *Proceedings of the Royal Society A: Mathematical,*  
582 *Physical and Engineering Sciences*, **464**, 777–793, doi: <https://doi.org/10.1098/rspa.2007.0277>.

583 Koper, K. D. & Hawley, V. L., 2010. Frequency dependent polarization analysis of ambient seismic noise  
584 recorded at a broadband seismometer in the central United States, *Earthquake Science*, **23**, 439–447, doi:  
585 <https://doi.org/10.1007/s11589-010-0743-5>.

586 Koper, K. D., de Foy, B., & Benz, H., 2009. Composition and variation of noise recorded at the yel-  
587 lowknife seismic array, 1991–2007, *Journal of Geophysical Research: Solid Earth*, **114**(B10), doi:  
588 <https://doi.org/10.1785/0120090120>.

589 Le Pape, F., Craig, D., & Bean, C., 2021. How deep ocean-land coupling controls the generation of

secondary microseism Love waves, *Nature Communications*, **12**, doi: <https://doi.org/10.1038/s41467-021-22591-5>.

Lecocq, T., Hicks, S. P., Noten, K. V., & et al., 2020. Global quieting of high-frequency seismic noise due to covid-19 pandemic lockdown measures, *Science*, **369**(6509), 1338–1343, doi: <https://doi.org/10.1126/science.abd2438>.

Li, L., Boué, P., Retailleau, L., & Campillo, M., 2020. Spatiotemporal correlation analysis of noise-derived seismic body waves with ocean wave climate and microseism sources, *Geochemistry, Geophysics, Geosystems*, **21**(9), e2020GC009112, doi: <https://doi.org/10.1029/2020GC009112>.

Liu, Q., Koper, K. D., Burlacu, R., Ni, S., Wang, F., Zou, C., Wei, Y., Gal, M., & Reading, A. M., 2016. Source locations of teleseismic P, SV, and SH waves observed in microseisms recorded by a large aperture seismic array in China, *Earth and Planetary Science Letters*, **449**, 39–47, doi: <https://doi.org/10.1016/j.epsl.2016.05.035>.

Liu, Q., Ni, S., Qiu, Y., Zeng, X., Zhang, B., Wang, F., Duan, Y., & Xu, Z., 2020. Observation of Teleseismic S Wave Microseisms Generated by Typhoons in the Western Pacific Ocean, *Geophysical Research Letters*, **47**(19), e2020GL089031, doi: <https://doi.org/10.1029/2020GL089031>.

Liu, Q., Zhou, Y., Ni, S., Xu, M., Qiu, Y., Zhang, Y., Yu, C., & Chu, R., 2024. Resolvability of Multiple Microseismic P-Wave Source Regions with Two Large Seismic Arrays in China and the United States, *Seismological Research Letters*, **95**(3), 1885–1898, doi: <https://doi.org/10.1785/0220230265>.

Longuet-Higgins, M. S., 1950. A theory of the origin of microseisms, *Philosophical Transactions of the Royal Society of London. Series A, Mathematical and Physical Sciences*, **243**(857), 1–35, doi: <https://doi.org/10.1098/rsta.1950.0012>.

Lu, Y., Pedersen, H. A., Stehly, L., & Group, A. W., 2021. Mapping the seismic noise field in Europe: spatio-temporal variations in wavefield composition and noise source contributions, *Geophysical Journal International*, **228**(1), 171–192, doi: <https://doi.org/10.1093/gji/ggab273>.

Lu, Y., Schmid, S. M., Wang, Q.-Y., & Bokelmann, G., 2023. Mapping the mantle transition zone discontinuities across south-central Europe using body waves from seismic noise correlations, *Earth and Planetary Science Letters*, **624**, 118457, doi: <https://doi.org/10.1016/j.epsl.2023.118457>.

McNamara, D. E. & Boaz, R. I., 2019. Visualization of the seismic ambient noise spectrum, in *Seismic Ambient Noise*, pp. 1–29, Cambridge University Press, Cambridge, U.K.

Nakata, N., Gaultieri, L., & Fichtner, A., 2019. *Seismic ambient noise*, Cambridge University Press.

Nishida, K. & Takagi, R., 2016. Teleseismic wave microseisms, *Science*, **353**(6302), 919–921, doi: <https://doi.org/10.1126/science.aaf7573>.

Nishida, K. & Takagi, R., 2022. A Global Centroid Single Force Catalog of P-Wave Microseisms, *Journal of Geophysical Research: Solid Earth*, **127**, doi: <https://doi.org/10.1029/2021JB023484>.

Obara, K., Kasahara, K., Hori, S., & Okada, Y., 2005. A densely distributed high-sensitivity seismograph

network in Japan:Hi-net by National Research Institute for Earth Science and Disaster Prevention, *Review of Scientific Instruments*, **76**, 021301–021301, doi: <https://doi.org/10.1063/1.1854197>.

Obrebski, M. J., Ardhuin, F., Stutzmann, E., & Schimmel, M., 2012. How moderate sea states can generate loud seismic noise in the deep ocean, *Geophysical Research Letters*, **39**(11), doi: <https://doi.org/10.1029/2012GL051896>.

Okada, Y., Kasahara, K., Hori, S., Obara, K., Sekiguchi, S., Fujiwara, H., & Yamamoto, A., 2004. Recent progress of seismic observation networks in Japan—Hi-net, F-net, K-NET and KiK-net, *Earth, Planets, and Space*, **56**, 15–28, doi: <https://doi.org/10.1186/BF03353076>.

Pedersen, H. A., Mattern, F., Poli, P., & Stehly, L., 2022. Imaging with seismic noise: improving extraction of body wave phases from the deep Earth through selective stacking based on H/V ratios, *Geophysical Journal International*, **232**(2), 1455–1467, doi: <https://doi.org/10.1093/gji/ggac388>.

Peterson, J., 1993. Observations and modeling of seismic background noise, *USGS Open File Report*, **93-322**, 94 pp.

Poli, P., Campillo, M., Pedersen, H., & LAPNET Working Group, 2012. Body-wave imaging of Earth's mantle discontinuities from ambient seismic noise, *Science*, **38**, 1063–1065, doi: [10.1126/science.1228194](https://doi.org/10.1126/science.1228194).

Retailleau, L. & Gaultier, L., 2021. Multi-phase seismic source imprint of tropical cyclones, *Nature communications*, **12**(1), 2064, doi: <https://doi.org/10.1038/s41467-021-22231-y>.

Retailleau, L., Landès, M., Gaultier, L., Shapiro, N. M., Campillo, M., Roux, P., & Guilbert, J., 2018. Detection and analysis of a transient energy burst with beamforming of multiple teleseismic phases, *Geophysical Journal International*, **212**, 14–24, doi: <https://doi.org/10.1093/gji/ggx410>.

Ruigrok, E., Gibbons, S., & Wapenaar, K., 2017. Cross-correlation beamforming, *Journal of Seismology*, **21**, 495–508, doi: <https://doi.org/10.1007/S10950-016-9612-6>.

Sager, K., Boehm, C., Ermert, L., Krischer, L., & Fichtner, A., 2018. Sensitivity of seismic noise correlation functions to global noise sources, *J. Geophys. Res.*, **123**, 6911–6921, doi: <https://doi.org/10.1029/2018JB016042>.

Shapiro, N. M., Campillo, M., Stehly, L., & Ritzwoller, M., 2005. High resolution surface wave tomography from ambient seismic noise, *Science*, **307**, 1615–1618, doi: [10.1126/science.1108339](https://doi.org/10.1126/science.1108339).

Shearer, P. M., Meng, H., & Fan, W., 2023. Earthquake detection using a nodal array on the san jacinto fault in california: Evidence for high foreshock rates preceding many events, *Journal of Geophysical Research: Solid Earth*, **128**(3), e2022JB025279, doi: <https://doi.org/10.1029/2022JB025279>.

Shen, W., Ritzwoller, M. H., & Schulte-Pelkum, V., 2013. Crustal and uppermost mantle structure in the central U.S. encompassing the Midcontinent Rift, *J. Geophys. Res.*, **118**, 4325–4344, doi: <https://doi.org/10.1002/jgrb.50321>.

Stutzmann, E., Ardhuin, F., Schimmel, M., Mangeney, A., & Patau, G., 2012. Modelling long-term seis-

661 mic noise in various environments, *Geophys. J. Int.*, **191**, 707–722, doi: <https://doi.org/10.1111/j.1365-246X.2012.05638.x>.

662

663 Tanimoto, T. & Anderson, A., 2023. Seismic noise between 0.003 Hz and 1.0 Hz and its classification,  
664 *Progress in Earth and Planetary Science 2023 10:1*, **10**, 1–22, doi: <https://doi.org/10.1186/S40645-023-00587-7>.

665

666 Tolman, H., Accensi, M., Alves, J.-H., Arduin, F., Bidlot, J., Booij, N., Bennis, A.-C., Campbell, T.,  
667 Chalikov, D., Filpot, J.-F., Foreman, M., Janssen, P., Leckler, F., Li, J.-G., Chawla, A., Lind, K., Orzech,  
668 M., Padilla-Hernandez, R., Rogers, E., & Zieger, S., 2014. *User manual and system documentation of*  
669 *WAVEWATCH III version 4.18*.

670 Tomasetto, L., Boué, P., Arduin, F., Stutzmann, E., Xu, Z., De Plaen, R., & Stehly, L., 2025. WMSAN  
671 Python Package: From Oceanic Forcing to Synthetic Cross-correlations of Microseismic Noise, *Seismica*,  
672 **4**, doi: <https://doi.org/10.26443/seismica.v4i1.1483>.

673 Xiao, H., Tanimoto, T., & Xue, M., 2021. Study of S-Wave Microseisms Generated by  
674 Storms in the Southeast Australia and North Atlantic, *Geophysical Research Letters*, **48**, doi:  
675 <https://doi.org/10.1029/2021GL093728>.

676 **APPENDIX A: SUPPLEMENTARY FIGURES**

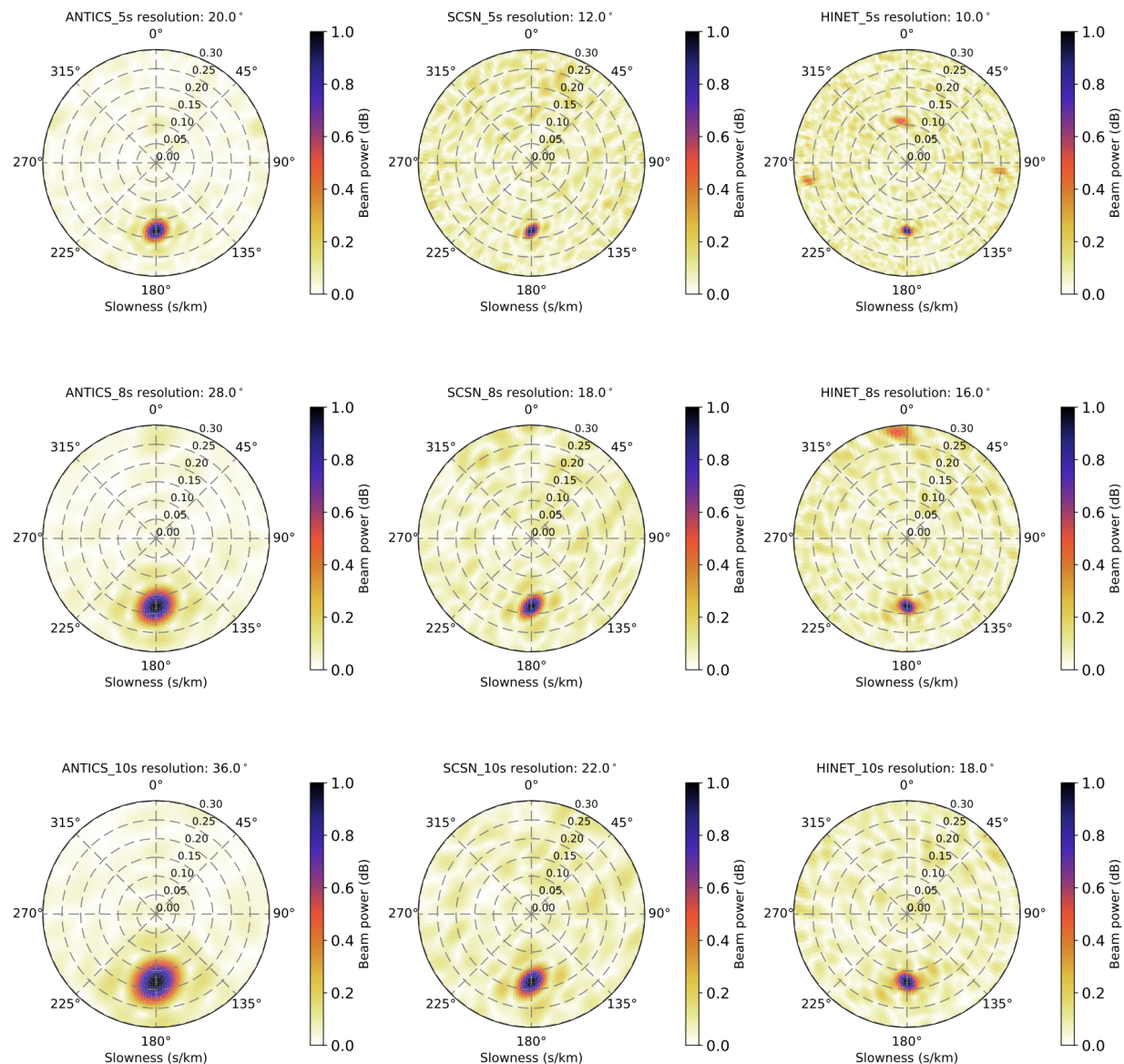


**Figure A1.** RA beamforming array response for a plane wave with slowness 0.15 s/km at 180° backazimuth. The header lines provide the -3 db (half-power) azimuthal beam widths as an estimate of backazimuth resolution.

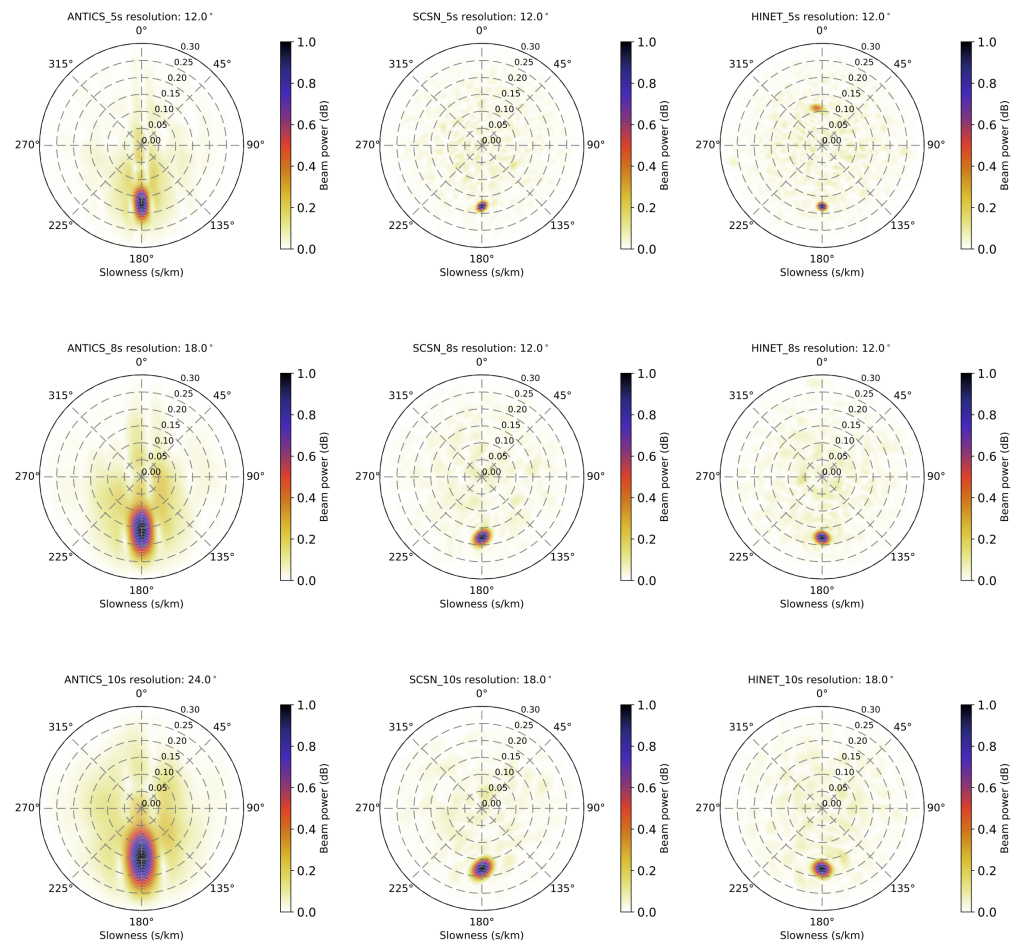


**Figure A2.** Three network cross-correlation beamforming array response functions for a plane wave coming with slowness 0.15 s/km at 180° backazimuth. The header lines provide the -3 db (half-power) azimuthal beam widths as an estimate of backazimuth resolution.

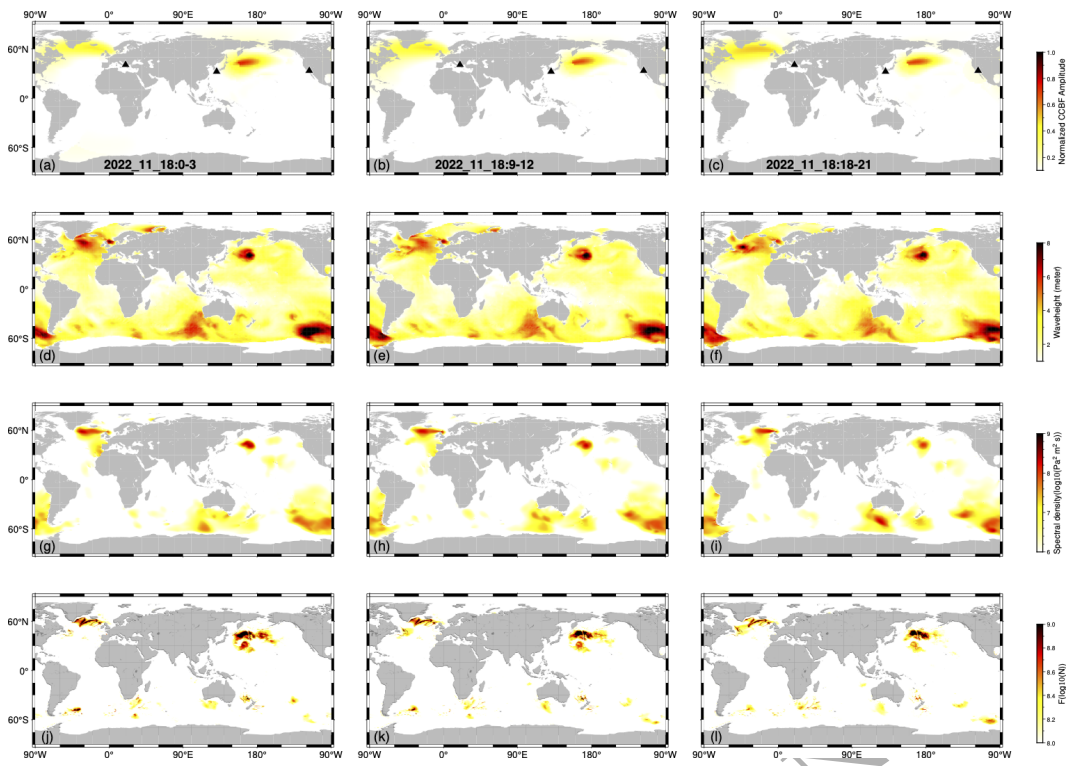


**Figure A3.** (a-c): Joint beam power map retrieved from the three networks based on 3-hourly cross-correlation stacks and their back-projection on 2022-11-18 for three selected times (see labels). (d-f): Corresponding significant wave height maps from WW3 model. (g-i): corresponding averaged PSD of the ocean surface pressure field from 5-10 s extracted from the WW3 model. (j-l): the equivalent vertical force applied at the seafloor calculated with the WMSAN code.

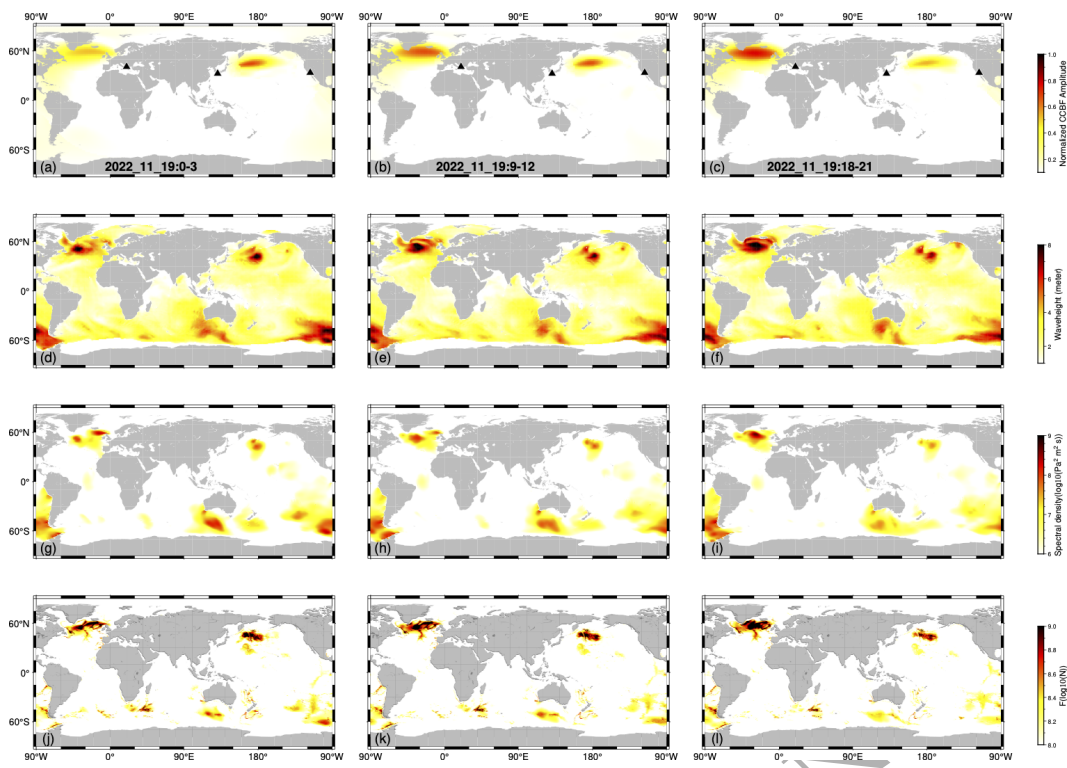


**Figure A4.** (a-c): Joint beam power map retrieved from the three networks based on 3-hourly cross-correlation stacks and their back-projection on 2022-11-19 for three selected times (see labels). (d-f): Corresponding significant wave height maps from WW3 model. (g-i): corresponding averaged PSD of the ocean surface pressure field from 5-10 s extracted from the WW3 model. (j-l): the equivalent vertical force applied at the seafloor calculated with the WMSAN code.

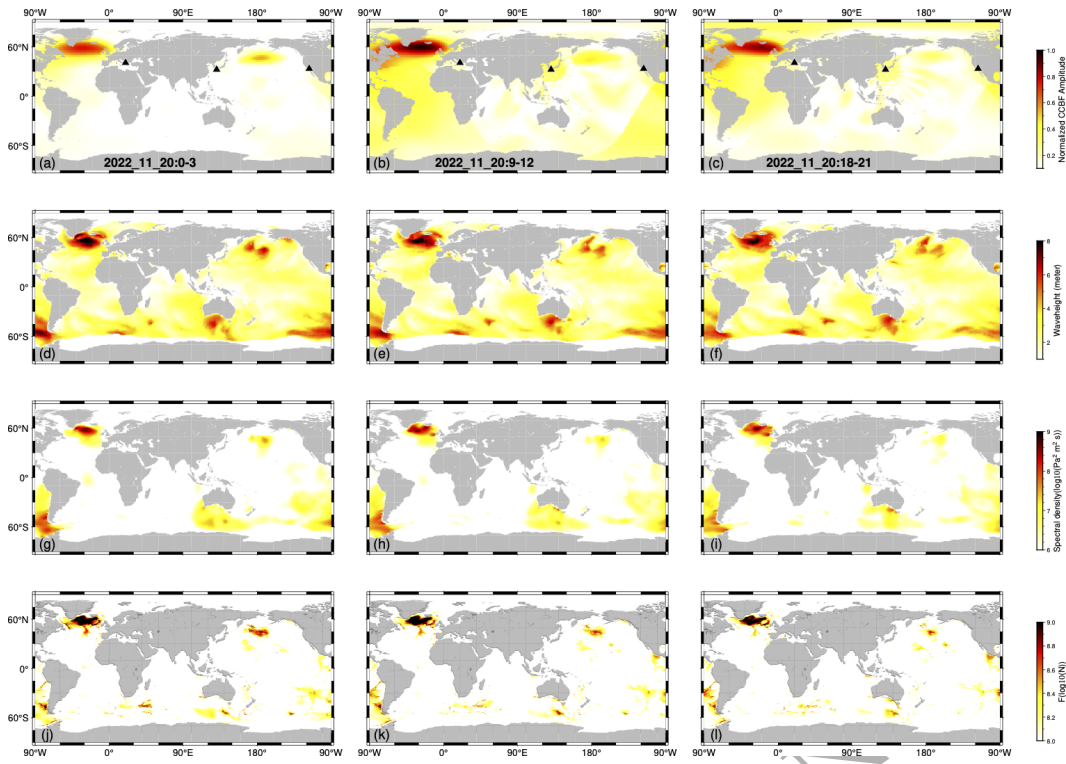


**Figure A5.** (a-c): Joint beam power map retrieved from the three networks based on 3-hourly cross-correlation stacks and their back-projection on 2022-11-20 for three selected times (see labels). (d-f): Corresponding significant wave height maps from WW3 model. (g-i): corresponding averaged PSD of the ocean surface pressure field from 5-10 s extracted from the WW3 model. (j-l): the equivalent vertical force applied at the seafloor calculated with the WMSAN code.

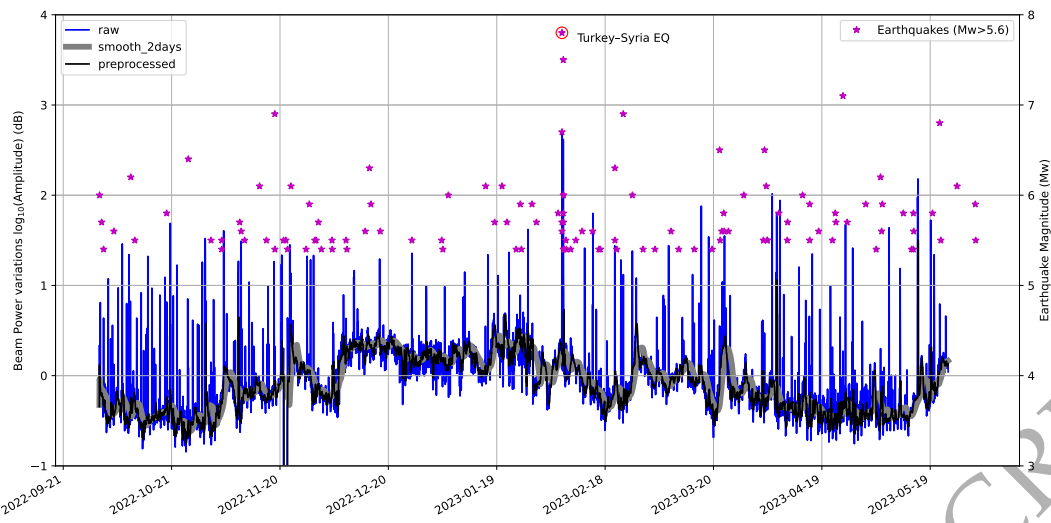


**Figure A6.** Comparison between the original beam power from RA beamforming and the preprocessed beam power. The fat grey line shows 2-day rolling mean and interpercentile range, 10<sup>th</sup> – 90<sup>th</sup> percentile (IPR). The outliers, typically caused by strong local, regional (especially February 2023 Turkey-Syria events), and teleseismic earthquakes, are excluded by the preprocessing, as detailed in the text.

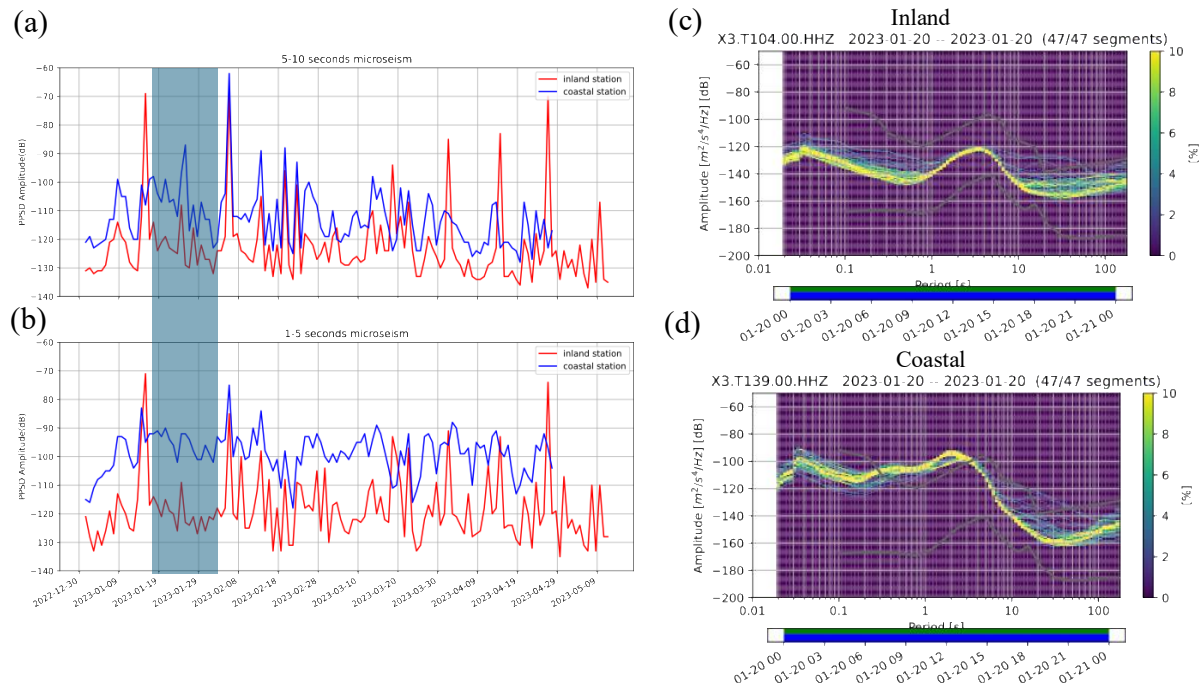


**Figure A7.** Comparison of noise characteristics at an inland ANTICS station (X3.T104) and a coastal ANTICS station (X3.T139). (a) Band-limited PSD amplitudes in the 5–10 s secondary microseism band (0.1–0.2 Hz) for December 2022–May 2023. The shaded area represents the date range of higher PPSD of coastal station than inland station, which also display mismatch of the smoothed raw data beam power and equivalent force. (b) PPSD amplitudes in the 1–5 s band for the same period. (c–d) PPSD distributions for a representative day (20 January 2023) show consistently higher spectral levels at the coastal station in the 0.1–0.2 Hz band, by 10–20 dB, compared to the inland site.

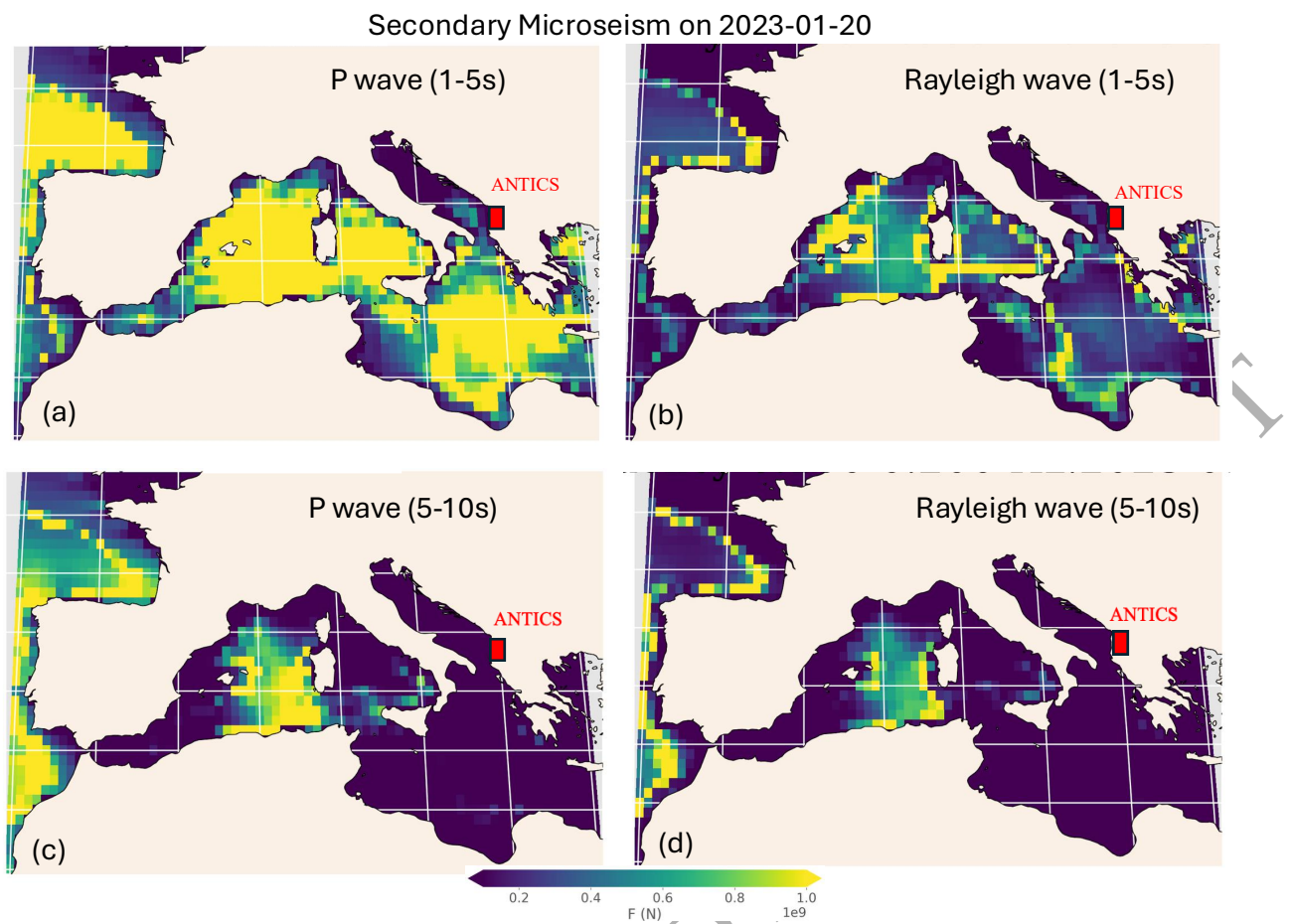
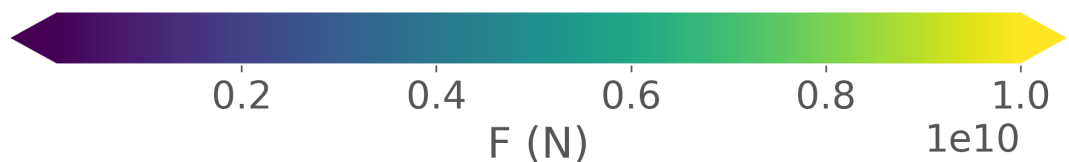
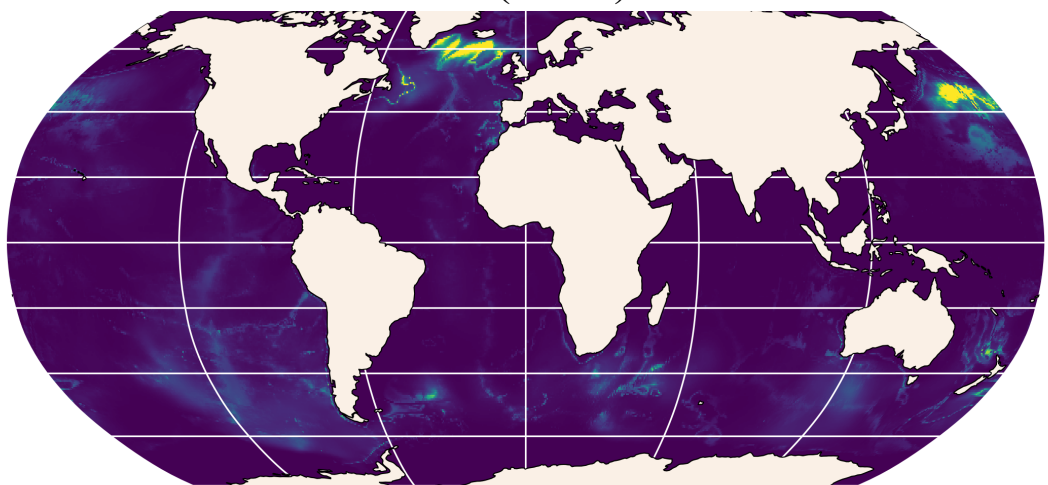


**Figure A8.** Computed P and Rayleigh wave secondary microseism sources (WMSAN) for the Mediterranean Sea on 2023-01-20. (a-b) 1-5 s (c-d) 5-10 s. The relatively weaker equivalent force of the microseism source of 5-10 s relative to 1-5 s also corresponds the elevated PPSD observed for the 1-5 s period from the inland station in Figure A7.

(a)

P wave (5-10s)



(b)

Rayleigh wave (5-10s)

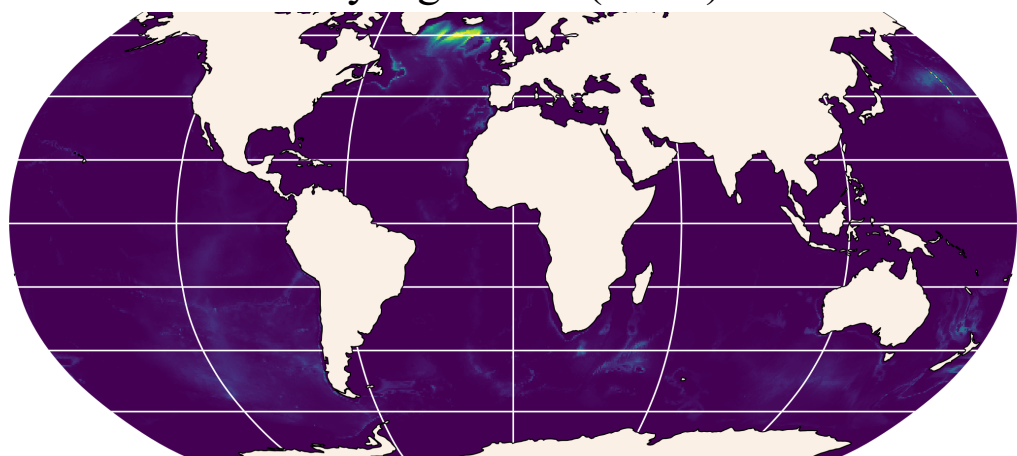


**Figure A9.** Computed global secondary microseism generation (WMSAN) on 2022-11-18. (a-b) 5-10s P wave microseism sources. (b) 5-10 s Rayleigh wave microseism sources.